Evaluation of the wavefronts and spatial structures of ultrashort pulses passing through a micro-channel plate

Simon Ek

Thesis submited for the degree of Master of Science
Project duration: 12 months

Supervised by Prof Johan Mauritsson and Neven Ibrakovic

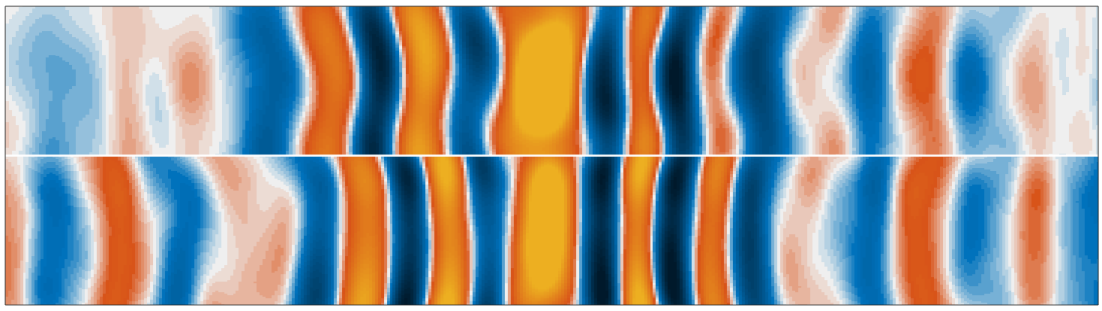

Department of Physics
Division of Atomic Physics

LRAP 551

January 2019

Evaluation of the wavefronts and spatial structures of ultrashort pulses passing through a micro-channel plate

Simon Ek

Supervisor: Johan Mauritsson

Co-supervisor: Neven Ibrakovic

Abstract

The first aim of this project is to make high-order harmonic (HHG) setups more compact and user-friendly, by including a micro-channel plate (MCP). Simulations of the transmission properties of an MCP has been performed. These simulations displayed introduced structure in the far field, but a very well behaved beam in the near field. Further, the wavefront of the zeroth order diffraction spot of MCP filtered extreme ultraviolet light from HHG, was measured, indicating that a negligible amount of distortion was introduced.

The second aim is to obtain understanding of the HHG process, utilizing a chirp scan technique. A measurement was performed, validating that chirp scans are equivalent to, the desired, intensity scans, for measuring quantum path interference (QPI) in HHG. Measured QPI plots show interference structures, which could only be simulated by adding a third interference source in an existing code. This could be the first measurement of a third quantum path in HHG. Finally, a chirp scan was performed with an MCP inserted in the setup. The resulting spectra and QPI plots show substantial off-axis artifacts, although retaining much of the on-axis behavior.

The findings of this project add to the knowledge of HHG and show that, even for very phase sensitive experiments, an MCP can be introduced to an HHG setup without compromising the obtained data.

Populärvetenskaplig sammanfattning

För att undersöka mycket snabba förlopp, likt elektroners rörelser kring atomkärnan, krävs ljuspulser som endast är några hundra attosekunder långa. En attosekund (10^{-18} s) är en miljarddels miljarddels sekund, och förhåller sig således ungefär till en sekund som en sekund förhåller sig till två gånger universums ålder.

Attosekundspulser, det vill säga ljuspulser kortare än en femtosekund (10^{-15} s), kan alstras med hjälp av en mycket intensiv infraröd laserpuls. När den intensiva och korta (ca 170 $\cdot 10^{-15}$ s) laserpulsen fokuseras i en gas så svarar gasen med att sända ut en eller flera ultrakorta (några hundra $\cdot 10^{-18}$ s) laserpulser som består av övertoner av den ursprungliga pulsens frekvens. Anledningen till att bara övertoner sänds ut är att alstringsprocessen sker ett stort antal gånger och att bara de frekvenser som är multiplar av den drivande laserns frekvens adderas konstruktivt. Alla andra frekvenser adderas destruktivt och släcks därmed ut.

Den genererade pulsen är som bäst en hundratusen-del så stark som den drivande och de två kommer att färdas i samma riktning. Det går därför inte att mäta den svaga genererade pulsen om den inte först separeras från den starka drivande pulsen. Att filtrera bort den drivande laserpulsen är därför en viktig uppgift.

Tidigare har man gjort detta med hjälp av extremt tunna, och därmed mycket sköra, metallfolier som reflekterar i den drivande pulsens frekvensområde, men är transparanta i den genererade pulsens frekvensområde. Ett problem med den här typen av filter är att de är otroligt ömtåliga och att man därför måste ha precis samma tryck på båda sidorna av filtret för att de inte omedelbart ska slitas itu. I det här projektet har vi undersökt om filtreringen istället kan göras med hjälp av en tunn glasskiva med tusentals små hål igenom, en MCP (multi-channel plate). Tanken är att de långa våglängderna i den drivande pulsen ska påverkas väldigt mycket i passagen genom plattan, medan de korta, genererade, våglängderna kommer passera genom hålen relativt opåverkade. Förenklat kan man säga att MCP:n fungerar på samma sätt som ett fiskenät. Ett nät släpper igenom små fiskar, men fångar de stora. På ett liknande sätt släpper en MCP igenom ljus med kort våglängd och "fångar" ljus av längre våglängd.

Tidigare har det visats att en MCP verkligen släpper igenom ljus med kort våglängd i större utsträckning än ljus med lång våglängd, men för att kunna använda den filtrerade ljuspulsen kan det vara nödvändigt att veta att den inte förändrats av MCP:n. I projektet har vi lyckats visa att vågfronten av den mest centrala delen av en ljuspuls inte förändras av att passera en MCP. Detta trots att ljuset i den centrala delen är summan av ett stort antal bidrag, där varje bidrag består av ljus som passerat MCP:n genom ett eget hål. När vi såg att ljuspulsen inte påverkades av MCP:n provade vi att upprepa tidigare experiment, men med en MCP i strålgången. Resultaten vi uppnådde var, i de centrala delarna, väldigt lika vad vi tidigare sett. Detta tyder på att det, även för väldigt faskänsliga experiment, kan vara en framkomlig väg att använda en MCP för filtrering av den drivande laserpulsen.

Acronyms

CCD Charge-coupled device

HHG High-order harmonic generation

IR Infrared

MCP Micro-channel plate

OPA Optical parametric amplifier

QPI Quantum path interference

RABBIT Reconstruction of attosecond beating by interference of two-photon transitions

XUV Extreme ultraviolet

Contents

1 Introduction

Extreme ultraviolet (XUV) light pulses were first obtained by high-order harmonic generation (HHG) in 1988 by Ferray et al. [1], but not until 2001 were their durations measured to be in the attosecond regime, by Paul et al. [2]. Ultra-short pulses, like these, are required to explore the dynamics of electrons in atomic and molecular systems, and has been utilized to do so ever since. It was, for example, shown in 2010, in an experiment using Neon, that the photoelectric effect comes with different time delays for different electron orbitals [3].

Since the first successful experiments the standard method to create attosecond pulses is HHG. It is initialized by focusing an intense laser pulse in a medium, e.g. a gas. The medium responds by sending out a train of attosecond pulses that co-propagate with the initial pulse. The driving pulse is often in the infrared (IR) or near-infrared part of the spectrum, while the generated pulse can reach into the XUV or higher. To be able to use, or even measure, the generated XUV pulse, the driving IR pulse has to be removed, since it is more than 100.000 times more intense than the generated pulse [4, 5, 6]. This can, for example, be done by spatially separating them with a grating or by using a thin metallic foil, which transmits part of the XUV and reflects the IR, as a filter. Two problems with such filters are that they will not transmit in the entire desirable spectral range and that they are extremely fragile.

The main goal of this project is to investigate the viability of a recently suggested IR removal method, which would address the problems mentioned above. The method is to install a micro-channel plate (MCP) in the HHG setup, something that would come with the additional benefit of reducing gas flow between the setup compartments. In 2014 it was proposed by Zhang et al. that an MCP can be used as a filter in HHG [7]. An MCP is just a thin (a few 100 μm) glass plate with multiple holes (on the order of 10 μm) through it. The holes are densely packed and can make up as much as 60 % of the surface of the plate. The reasons that MCP filters could solve the problems of previous filters, are that they are much more rigid than thin metallic foils and that they do not discriminate between wavelengths as metals do. It was found that the driving laser can be partly blocked by installing an MCP in the beam line. The physics relied upon when using an MCP as a filter in HHG, is that when interacting with the MCP, the long wavelengths of the driving pulse will diffract much more, than the short wavelengths of the generated pulse. Hence, MCP will work as a high pass filter. In the 2014 paper it is indeed shown that shorter wavelengths have a higher transmission rate than the long wavelength.

Further, the researchers showed that an MCP filtered XUV pulse can be used in reconstruction of attosecond beating by interference of two-photon transitions (RABBITT) scans. In these scans the generated XUV is focused into a target gas together with a fraction of the driving IR pulse, and the energies of the resulting photoelectrons are measured, as the delay between the two pulses are scanned. Since the XUV is focused in such an experiment, the well behaved RABBITT scans only show that the spatial phase profile of the near field (focused) beam is well behaved. Whether or not the same is true in far field is not answered in the article. It might be that there is a distortion in the wavefront, which is only seen when the beam is

unfocused. One of the goals of this project is to answer that question; is the MCP filtered wavefront well behaved in far field?

In HHG each obtainable photon energy can be reached by more than one quantum path, meaning that within a particular energy, i.e., harmonic order, interference between these quantum paths can occur. Measuring these interferences is non-trivial, but with our setup and the right data analysis the interference patterns can be quite distinguishable. By observing these interference patterns and how they change when the generation conditions are varied, knowledge about the light-matter interaction that is at the core of HHG can be gained. Therefore, a secondary goal of this project is to expand that knowledge by doing chirp scans, in which the intensity of the driving IR pulse is changed by stretching or compressing it in time.

2 Background

In the background section the concepts that are needed to understand the motivation and to explain and discuss the results will be laid out. More precisely the HHG process will be described with a focus on phase matching and the different trajectories. Furthermore, a Matlab code that simulates propagation of generated harmonics from near field to far field will be described. First the possible benefits an MCP could have on the setup in question for this project will be explained.

2.1 Benefits of an MCP

The HHG setup used in this project is very small and user-friendly, compared to most other HHG systems. It does not require daily re-alignment, can easily be run by one person, has an industrial laser that is turned on by flicking a switch, and does not measure more than two meters from laser to detector. The system is built with the expressed intention to be easy to use, stable and cheap. The trade-off is that it neither deliver the shortest nor the most intense pulses.

This setup would not benefit from the IR filtering ability of an MCP, but rather from its ability to block the generation gas in the generation chamber from seeping into the detection chamber. The reason that this is desirable is that it decreases the wear on the high voltage MCP detector. In the setup there is no need to block the IR since most of it is blocked when the beams pass through a 1 mm pinhole after generation, and the rest is spatially separated from the XUV by a grating. However, if an MCP could be put between the generation and detection chamber it would help preventing gas from leaking into the detection chamber. This would reduce the need for differential pumping, which is the practice to pump consecutive vacuum compartments individually, and thus gradually decrease the gas pressure towards the detector. For differential pumping to be effective the resistance to gas flow between compartments must be high, and installing an MCP would contribute to that. This could then mean that the setup could work with only one 10.000 $ turbo pump, instead of two, or that the lifetime of the 50.000 $ MCP used for detection is extended. Removing a turbo pump from the setup would not only save money, but more importantly, it would remove a part that can fail

and/or add noise to the experiments, thus making the setup more robust and easier to maintain.

2.2 High-order harmonic generation

HHG is a highly non-linear process where an ensemble of atoms is irradiated by a high intensity laser and as a response emits harmonics of the driving laser light. The process was first discovered in 1977, using a solid target [8]. In the late 80's, two independent research groups observed high harmonics, using a gas target [9, 1]. In previous, ordinary, harmonic generation experiments the intensity decreased rapidly with the harmonic order, but what was seen in the late 80's saw was something completely different. They found a spectrally broad plateau region where the intensities of the harmonics were approximately constant, followed by a cut-off region where the intensities dropped-off fast. This very behavior can be seen in figure 1, which contains experimental data from HHG in Argon with a 1030 nm wavelength laser. The figure consists of an acquired spectrum, as seen by the camera, and overlaid that an intensity spectrum that shows the relative strength of the individual harmonics. As seen, each harmonic consists of an intense central part surrounded by a dimmer and more divergent part. The central and outer parts are the results of, what are called, the short and long trajectories, respectively. For harmonic 21 a clear ring-structure can be seen in the long trajectory part, which is thought to be due to interference within the long trajectory contribution [10]. Under the right circumstances this phenomenon can also be seen for the other harmonics, but not very clearly in this particular spectrum. In the region where long and short trajectory overlap, interference between the two can be observed, e.g. using the technique described in section 3.4.

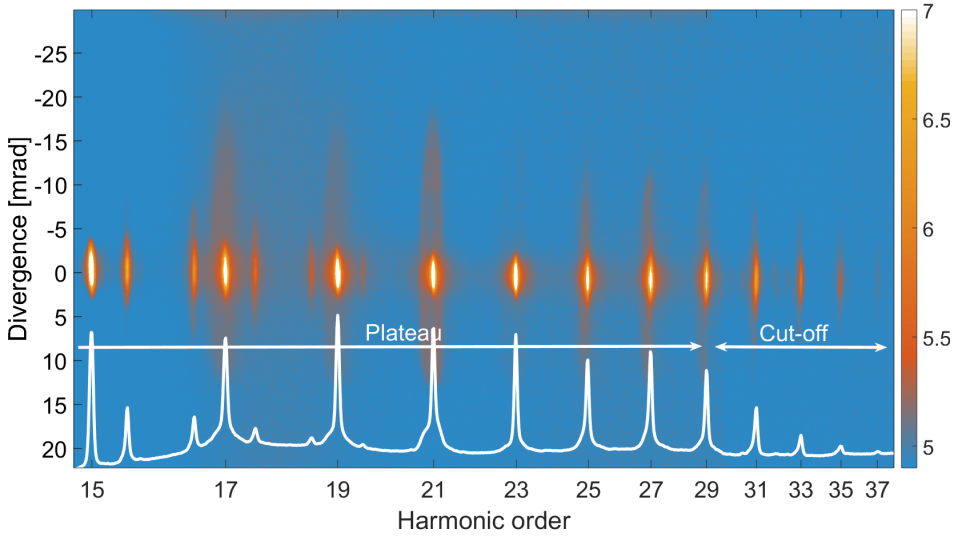

Figure 1: A spectrum obtained using HHG in Argon. In the lower part the intensity of each frequency component is plotted. The plateau region, with similar harmonic intensities, and the cut-off region, where the intensity rapidly drops, are indicated by arrows. The small peaks in between the harmonics are second order diffraction spots.

2.2.1 The tree-step model

The time-dependent Schrödinger equation can be used to replicate the experimental results seen in figure 1, but to actually understand the observed behavior, a simpler - more intuitive - model is needed. The three-step model is precisely that. It is a semi-classical model that was developed in the early 90's, and it is both simple and gives an explanation for the plateau and the cut-off regions [11, 12]. As indicated by the name, the model consists of three steps: (*i*) ionization by tunneling, (*ii*) acceleration in the laser field, and (*iii*) recombination. The first and last of these steps are quantum mechanical to their nature, while the second is purely classical; hence the label semi-classical. Each of the steps can be found in figure 2, where they are indicated by (*i*) - (*iii*), and will be explained in more detail below.

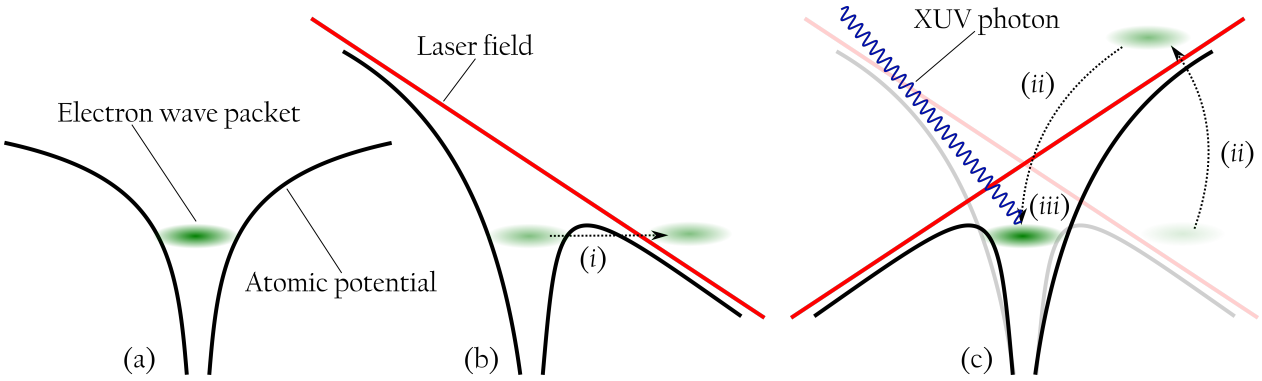

Figure 2: A schematic overview of the three-step model. In (a) the electron sits in the atomic potential, in (b) part of the electron wave packet tunnels out, and in (c) the ionized part of the electron wave packet is first accelerated in the laser field, and then driven back to recombine with the part that remained in the atomic potential, releasing its excess energy as a photon.

The first step (*i*) is for part of the electron wave packet to tunnel out of the atomic potential. This is only possible if the atomic potential is distorted enough by an external field, so that a barrier forms, through which the electron can tunnel to a state of equal or lower potential energy. For this to happen the amplitude of the external field must be of the same order as the Coulomb field that attracts the electron to the nucleus, forming the atomic potential. In practice this means that a laser field must have an optical intensity approaching 10^{14} W/cm^2, to make tunneling possible [13]. What actually tunnels out is not the entire electron, but rather a part of the electron wave packet, which gives the probability of finding the electron in a certain position.

As part of the electron has tunneled out it will move freely in the external electromagnetic field and be accelerated by it. This is step two (*ii*). Since this step is considered to be classical the electron wave packet will be treated as a particle at the position of highest probability and called just "the electron". Further, we will only consider the electric part of the field, ignoring the magnetic part, and assume that the field is perfectly linearly polarized, so that the electron only moves in the y direction. Finally, we assume that the kinetic energy of the electron is zero immediately after tunneling. The position of the electron can then be found by solving Newton's equations of motion, and with a laser field that varies sinusoidaly it will be

$$y(t) = \frac{eE_0}{m_e\omega_0^2}[sin(\omega_0 t) - sin(\omega_0 t_i) - \omega_0(t - t_i)cos(\omega_0 t_i)], \tag{1}$$

where e and m_e are the charge and mass of the electron, E_0 and ω_0 the amplitude and angular frequency of the electric field, t is the time, and t_i is the time of tunneling (ionization) [14, p. 40]. Taking the derivative of equation 1 with respect to t the velocity of the electron is obtained:

$$v(t) = \frac{eE_0}{m_e\omega_0^2}[cos(\omega_0 t) - cos(\omega_0 t_i)]. \tag{2}$$

The final step is recombination (*iii*), where the free electron is driven back to its initial state in the atomic potential and releases its excess energy as a photon. The photon frequency will depend on the kinetic energy of the returning electron and can reach in to the XUV part of the spectrum. From here on the resulting light from HHG will be called XUV light, even if it happens to be less energetic.

Recombination can only happen if the electron actually returns to its ion at $y = 0$, i.e., if equation 1 has a non-trivial ($t_r \neq t_i$) solution for $y(t_r) = 0$, where t_r is the return time. This equation can be solved analytically, and that results in the trajectories seen in figure 3. Each solution will be associated with a velocity that is given by equation 2, and hence with a return energy

$$E_r(t_i) = \frac{m_e v(t_r)^2}{2} + I_p = 2U_p[cos(\omega_0 t_r) - cos(\omega_0 t_i)]^2 + I_p, \tag{3}$$

where t_r is given by t_i,

$$U_p = \frac{e^2 E_0^2}{4m_e\omega_0^2}$$

is the ponderomotive energy, i.e., the average kinetic energy of an electron moving freely in the oscillating field, and I_p is the ionization potential. The trajectories in the figure are colored according to their return energy and the trajectory with the very highest return energy is marked with a black line. Trajectories inside of (closer to zero than) this line are called short, and those outside are called long. The arrows represent the direction and amplitude of the driving electric field.

Only ionization events - and following trajectories - during the first half cycle are shown, but the process repeats itself every half cycle. The direction of the trajectories will be opposite for consecutive half cycles, due to the field changing sign. In the figure, one can see that during the first quarter cycle the freed electrons do not return, and in the second quarter they first return along the long trajectories and then along the short trajectories. Since it is part of an electron wave packet that travels the trajectories, even among those trajectories that pass through $y = 0$ only a small fraction actually lead to recombination, most just continue on. In the lower part of the spectrum are trajectories that are a result of wave packets that could have recombined but did not. Out of these some never pass the nucleus again (grey), while others do. Of those that do pass the nucleus a second time some recombine and are colored according to their recombination energy. This means that there could possibly be more than just short and long trajectory, namely trajectories

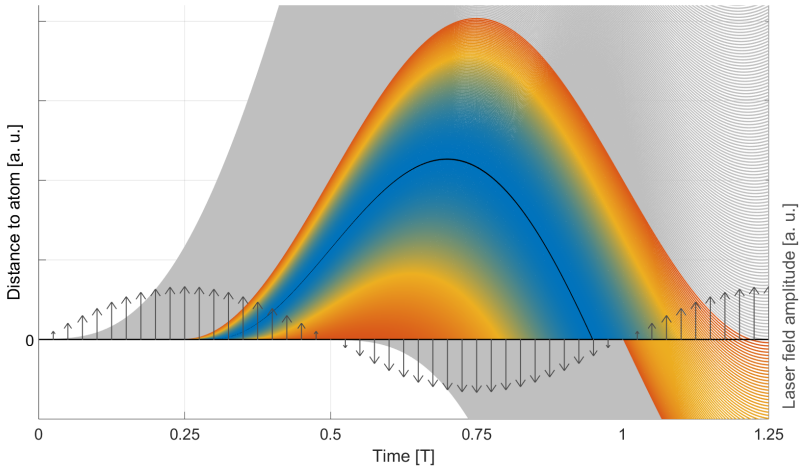

Figure 3: Classically calculated electron trajectories for HHG. Grey trajectories do not return to the mother atom. The returning trajectories are colored according to their return energy; red for low energy and blue for high energy. The black line mark the trajectory with the highest possible return energy, and trajectories inside (outside) of it are called short (long). The driving electric field is represented by arrows.

resulting from wave packets that did not recombine on the first passage through $y = 0$, but maybe on the second (or higher) passage. To the authors knowledge no such longer than long trajectories has yet been measured, but have been theoretically predicted [13].

Plotting the recombination energy as a function of return time, as in figure 4, shows that the highest reachable energy is $3.17U_p + I_p$, and the fact that there is a highest energy explains the cut-off in figure 1. Every energy below the cut-off can be reached by both a long and a short trajectory, but not all energies can be reached by possible longer trajectories. It is worth pointing out that since U_p increases linearly with the driving field intensity, the cut-off can be shifted by adjusting the intensity of the driving laser. From figure 3 it is not possible to say that any of the reachable energies should be preferred over any other energy, which is in accordance with the observed plateau-region.

The simple model outlined above succeeds in explaining why there is a cut-off in the observed frequencies, and is fully compatible with a plateau-region. It also explains why each observed harmonic contains two distinct parts - long and short trajectory. However, to this point it does not explain why only the odd harmonics, and not all frequencies up to the cut-off, are observed.

2.2.2 Multiperiodic effects

If the XUV light that is generated during one specific cycle is separated from the light that is generated during other cycles, the response would not be discrete harmonics (even though the process would still go under the HHG label), but rather a continuous spectrum. A separation of consecutive pulses can be achieved using a technique called non-collinear optical gating [15], but unless any special technique is applied the response will be that of a multiperiodic process, where only the odd harmonics are present in the resulting

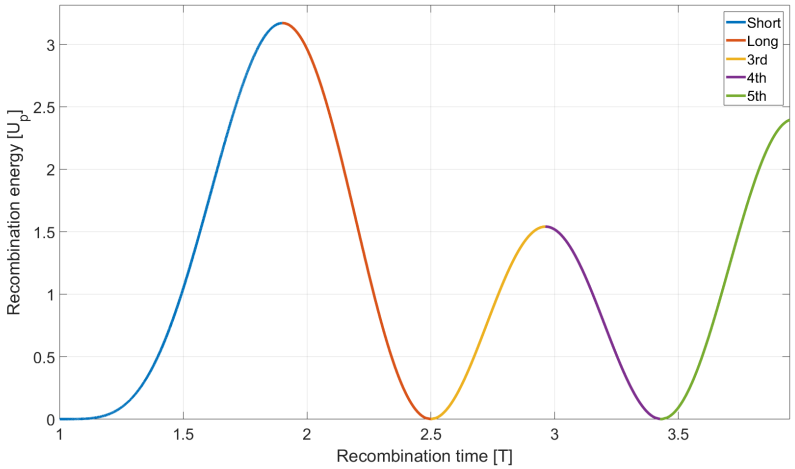

Figure 4: Recombination energies as function of recombination time.

XUV emission.

This being the case can be seen by examining the superposed electric fields of several emission events of a certain frequency $a\omega_0$. As seen in equation 3 this particular frequency is associated with a specific return time $t_r^{(a)}$. The frequency in question will be emitted again every $T/2$, i.e., light of frequency $a\omega_0$ will be sent out every $t_r^{(a)} + bT/2$, where b is an integer. Consecutive emission events will have a phase difference of π, due to the driving field changing sign. For simplicity we assume that the emitted field propagates with exactly the same speed as the driving field, so that no extra phase is introduced between consecutive emission events. The total electric field from n emission events will then be the real part of

$$\begin{aligned}
\tilde{E}_{tot}(t) &= \sum_{b=0}^{n-1} E_0 e^{ia\omega_0(t+bT/2)} e^{ib\pi} \\
&= E_0 e^{ia\omega_0 t} \sum_{b=0}^{n-1} e^{ia\omega_0 bT/2} e^{ib\pi} \\
&= E_0 e^{ia\omega_0 t} \sum_{b=0}^{n-1} e^{i\pi b(a+1)} \\
&= E_0 e^{ia\omega_0 t} A(a,n)
\end{aligned}$$

where $\omega_0 T = 2\pi$ and the sum has been named $A(a,n)$ in the last step. $|A(a,n)|$ is the relative amplitude of the frequency $a\omega_0$ and is plotted as a function of a for three different n's in figure 5. As seen, all frequencies - except for the odd harmonics - will be increasingly suppressed as the number of periods, n, that HHG occurs over is increased. When n becomes large, the multiperiodic response pulse will only contain frequencies $q\omega_0$, where q is an odd integer, i.e., it will only contain the odd harmonics of the driving field. This is exactly what is seen in figure 1, where the spatial separation according to frequency results in discrete bright spots.

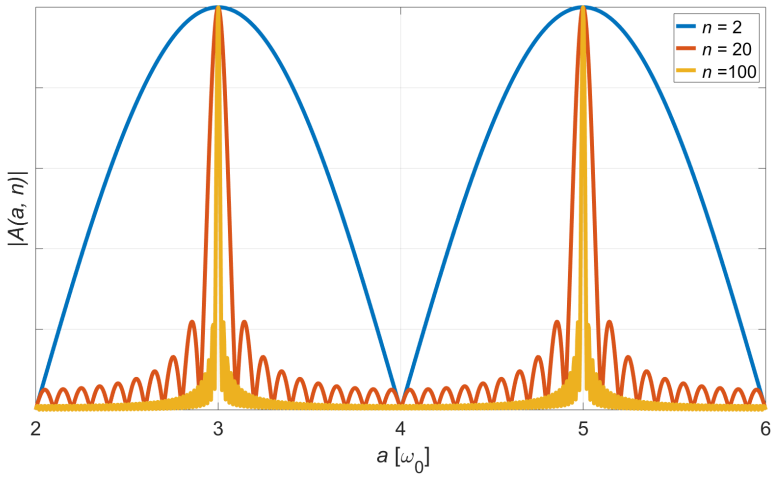

Figure 5: The relative intensities for frequencies from harmonic 2 to 6 in multiperiodic HHG. All the curves have been normalized individually.

2.2.3 Phase matching and interference effects

To achieve a high XUV yield the individual atoms that make up the interaction medium must emit in concert, i.e., in a way that makes their individual emissions add up constructively [16]. This is called phase matching. The wave vector mismatch, Δk, is a measure of how well phase matching is achieved, with a perfect phase match occurring when $\Delta k = 0$. Δk can be expressed as a sum of separable terms, each being the result of a physical phenomenon:

$$\Delta k = \Delta k_g + \Delta k_d + \Delta k_n + \Delta k_p. \tag{4}$$

The first term, Δk_g, results from the Gouy effect. This effect is geometrical in its origin and means that there is an additional term - compared to a plane wave - added to the phase of a Gaussian beam that goes through a focus. The term is $\zeta(z) = \text{atan}(z/z_0)$ and varies from $-\pi/2$ at $z = -\infty$ to $+\pi/2$ at $z = +\infty$, with z being the position on the optical axis and z_0 being the Rayleigh range [17, p. 77 - 81]. Since the generated XUV field inherits the phase of the driving field the Gouy effect will contribute to the wave vector mismatch and along the optical axis it will be:

$$\Delta k_g = \frac{d\zeta(z)}{dz} \tag{5}$$

[14, p. 45]. Close to the focus this derivative can be considered constant, with respect to z.

The second term is the dipole term, Δ_d, which arises in the interaction between the driving field and the atom. As described in section 2.2.1, a certain XUV frequency is associated with the electrons recombining at a particular instant of the driving field cycle, and hence the resulting XUV photon inherits a certain phase

from the driving field. This is however only true for constant intensity, I, of the driving field. So, if the intensity is changed, that same frequency will be generated at a different instant of the driving field cycle, and, consequently, inherit a different phase. This term therefore depends on intensity variations over the focus, and along the optical axis we have:

$$\Delta k_d = -\alpha_q^{(s,l)} \frac{dI(z)}{dz}, \tag{6}$$

where $\alpha_q^{(s,l)}$ is a constant that depends on the kind of trajectory (long or short) and on the harmonic order, q. α is generally larger for long trajectories, which has to do with the long trajectory electrons spending more time in the continuum and therefore being more sensitive to changes in tunneling and recombination times, and hence to intensity variations. In practice this means that if a short focal length is used to focus the IR, Δk_d will be large, and has to be compensated for with the other three terms to achieve a high XUV yield.

The divergence of the generated XUV light is also related to, the newly introduced, α. To see how this value affects curvature one should look at the phase variation over the plane of focus (the plane perpendicular to the optical axis at the focus). The phase, ϕ, is to first approximation connected to the intensity I of the driving field by the equation:

$$\phi^{(s,l)}(r) = \alpha^{(s,l)} \cdot I(r), \tag{7}$$

where r is the radial position [18, p. 41]. As seen, α appears in this equation, as well. In [14] the more precise relation

$$\phi^{(s,l)}(\Omega) = \alpha_0^{(s,l)} I + \beta^{(s,l)}(\Omega - \Omega_p) + \frac{\gamma^{(s,l)}}{I}(\Omega - \Omega_p)^2, \tag{8}$$

where α_0, β and γ are constants, Ω is the frequency of the generated light, and Ω_p is the frequency corresponding to ionization, is used instead.

Since the intensity of the driving laser is - at least approximately - varying as a Gaussian along the radial axis, the long trajectories greater sensitivity to intensity changes also means that the phase will vary more rapidly along the radial axis for the long trajectories. This would result in the wavefronts of the long trajectories accumulating more curvature, and hence the long trajectory emission being more divergent. The greater divergence is seen as long trajectory contribution being more stretched out along the y axis in figure 1.

Now it has been established that the same harmonic frequency can be reached by two different quantum paths, i.e., long and short trajectories, and that these paths accumulate phase differently, in accordance with their different α's. α is the parameter that connects the accumulated dipole phase to the intensity of the driving laser at generation. This means that in areas where long and short trajectory overlap their interference can vary from constructive to destructive, as the intensity of the driving laser is scanned. How fast this interference oscillates between constructive and destructive depends on $|\alpha^l - \alpha^s|$, and the contrast

of the interference depends on their relative field amplitudes, in the area of interest. As the harmonic order increases α^s and α^l converges to the same value, and, hence, the interference of long and short contributions becomes independent of the driving laser intensity [10]. This behavior can be predicted by just looking at figure 3 and noting that the higher the return energy the more similar are the trajectories of long and short, and hence the intensity dependence of their phases should also be more and more similar.

The third and fourth terms in equation 2.2.3 are due to the driving IR field and the generated XUV field not having the same refractive indices. This means that the driving and generated fields propagate at different speeds in the medium, and hence a phase difference will be introduced between consecutive emission events. In particular, the third term is due to the refractive index difference in the neutral gas, while the fourth term is the equivalent in plasma. The plasma term is more important for higher intensities, as more electrons are liberated, and hence more plasma created, in those cases. The terms are:

$$\Delta k_n = q\frac{\omega_0}{c}(n_1 - n_q) \tag{9}$$

and

$$\Delta k_p = q\frac{\omega_0}{c}(n_1^e - n_q^e), \tag{10}$$

where c is the speed of light in vacuum, n_1 (n_1^e) is the refractive index of the driving field in the gas (plasma), and n_q (n_q^e) is the refractive index of the q'th harmonic in the gas (plasma) [19, p. 61].

2.3 Simulation of far field propagation

The long-short interference described in the end of section 2.2.3 can be measured, and the measurements could potentially provide insights about how the phase accumulation of the different trajectories actually depend on the driving laser intensity. A geometrical code that simulates HHG with adjustable generation parameters and propagation of XUV harmonics from near field, where they are generated, to far field, where they can be observed, has been developed for this purpose [10]. In the code it is assumed that the harmonics are solely generated in the focal plane of a cylindrically symmetric driving IR field. In accordance with section 2.2.3, the phase profile of the harmonic is hence only dependent on the intensity profile of the IR, and is given by equation 7 at each radial position. Since HHG is a highly non-linear process, meaning that small changes in the driving field amplitude, A_{IR}, results in large changes in the amplitude of the generated field, the amplitude of the XUV is assumed to be A_{IR}^N. For harmonic q the field at generation is thus:

$$U^{(s,l)}(r) \propto A_{IR}^N(r) \cdot exp[i\alpha_q^{(s,l)} A_{IR}(r)], \tag{11}$$

where N is a non-linearity parameter that is greater than 1, which reflects the intensity dependence of the generation efficiency. N is potentially different for every trajectory and harmonic, and a larger N means that generation is confined to a smaller area.

Looking at a central lineout of the generation plane the IR phase, IR amplitude, XUV phase and XUV amplitude will be as in figure 6. In reality the XUV amplitude will be much smaller than the IR amplitude, but here they are both normalized. Since we look in the plane of focus the IR phase is flat and can be considered zero. Hence, it will not add to the XUV phase, which has a linear relation to the IR amplitude.

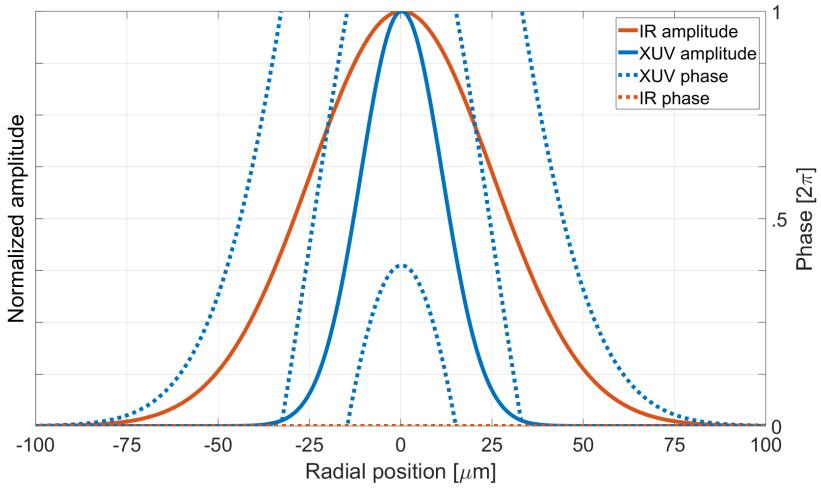

Figure 6: The amplitude and phase of the driving IR field and the generated XUV field.

As the field is defined at generation it can be propagated to far field using the Fourier transform [18, p. 133]. To this point everything in the code has been one-dimensional, but by changing the driving IR pulse duration and repeating the process multiple times, a two-dimensional matrix is being built up, column by column. The changes in pulse duration will also affect the pulse amplitude, and thus intensity.

After completing the process for all the desired intensities it is repeated, but with a new α, simulating the contribution from another electron trajectory interfering with the first contribution. In total this makes up a simulation of a chirp scan, where the intensity of the driving pulse is scanned by changing the pulse duration, as described in section 3.4. A typical result of a simulation can look something like what is displayed in figure 7. In principle more contributions could be added.

3 Methods

The project is divided in two main directions: one part that is solely about the MCP and the way it effects coherent light that passes through it, and a second part that concerns chirp scans, i.e., QPI experiments. As described in the introduction, it would be beneficial if the setup used for the QPI experiments could be equipped with an MCP. The question is whether or not that would compromise the obtained results.

The connection between these two parts will be a comparison of the results of QPI experiments with and without an MCP in the setup. If they turn out similar it would indicate that it is possible to use MCP filters in setups intended for far field applications where the sensitivity to the phase of individual electron trajectory

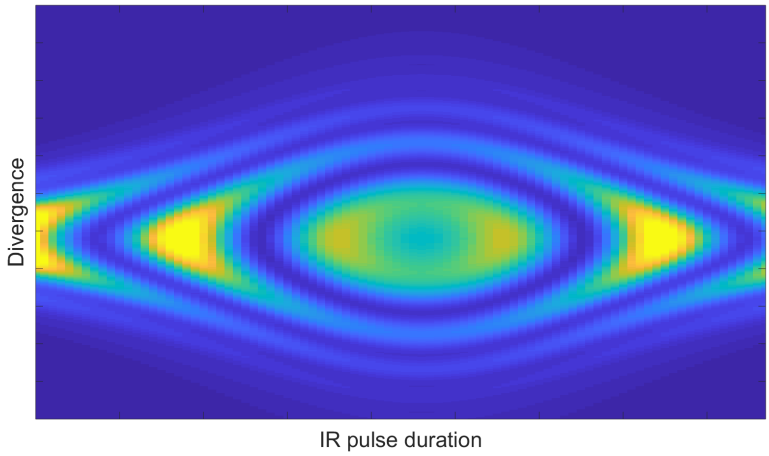

Figure 7: An example of the results obtained by simulating far field propagation of two interfering trajectories.

contributions are very high.

In this section the MCP experiments and simulations will be described first, followed by the QPI experiments.

3.1 Simulating an MCP filter using FRED

For all the simulations the ray tracing program FRED from Photon Engineering was used. The program offers the possibility to trace rays from both incoherent and coherent light sources through an optical system and extract the intensity recorded on a detector, for further analysis.

The setup that was used for modeling propagating laser through an MCP can be seen in figure 8a. At (a) is the light source, a coherent point source, called "Laser Diode Beam" in FRED. The divergence of the source can be varied and was set to either $0.29° \approx 5$ mrad or $1.15° \approx 20$ mrad, when simulating emission from short and long trajectories, respectively. The divergence is defined as the half width angle where the power has decreased to $1/e^2$ of the maximum power. The chosen angles are somewhat arbitrary, but correspond relatively well with divergence angles seen in earlier experiments; see, for example, figure 1 in [20] and figure 1 in this thesis. The beam profile of the source is Gaussian.

The model of the MCP filter itself is the blue circle at (b), and it consists of two planes, an input plane and an output plane. At the input plane the positions of the holes that are needed in the simulations are found, as well as an analysis surface that registers the incoming light. In the program an analysis surface is an non-interacting surface that can be attached to other surfaces to allow read out of incoming rays. The hole positions can be seen in figure 8b, where they are marked by circles of the same size as the holes of a real MCP would be. At the output plane is an analysis surface identical to the one on the input plane. The analysis surfaces are made to cover all the holes and have 257 by 257 pixels. The size of each analysis

surface had, hence, to be increased when using 20 mrad divergence for the beam, compared to when using 5 mrad. The distance between the planes were set to 400 μm and the hole diameter to 10 μm, giving a plate thickness to hole diameter ratio of 40:1. The number of rays across the beam was set to 65.

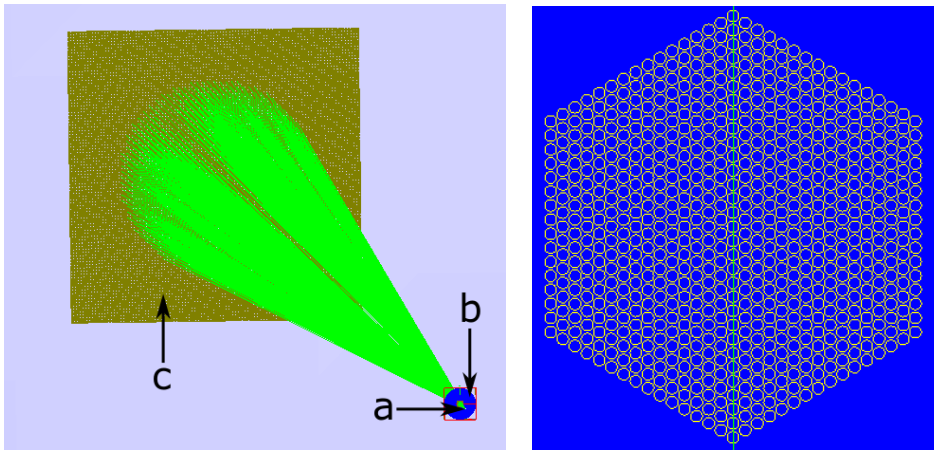

(a) The setup consists of (a) a coherent point source, (b) an MCP model, and (c) a detector.

(b) The 721 hole positions of the MCP input plane.

Figure 8: The setup used for the simulations in FRED.

The detector, at (c), consists of a plane and a 401 by 401 pixel analysis surface. This resolution is insufficient to resolve the finer details of the entire interference pattern, and therefore the analysis surface was offset to just cover one quadrant; effectively doubling the resolution in each direction. The complete pattern was later reconstructed from the recorded pattern. This could be done since the setup is perfectly mirrored by both the central vertical plane (x = 0) and the central horizontal plane (y = 0). The expected symmetry was also seen when the analysis surface was set to cover the entire detector. Just doubling the resolution to 801 by 801 was not a feasible option, since the computation time scales with the number of pixels and hence would have been approximately four times longer in that case.

As light hits the input plane it is detected by the corresponding analysis surface and stored as a two dimensional intensity distribution. A circular aperture with diameter $d = 10\,\mu$m is then moved to the first hole position. From the detected intensity distribution, rays that emerge from within the aperture are then re-synthesized and emitted towards the output plane. These secondary rays are in turn detected at the output plane. At the output plane an identical aperture is moved to the same x and y position as the aperture at the input plane. Rays are then re-synthesized a second time, this time at the output plane. The rays from the output plane reach the detector 600 mm away from the MCP. At this point the transmittance of light through one hole has been simulated. The process is repeated for each hole, making the interference pattern slowly build up at the detector. With this method it is not possible to include reflections within the channels.

With the computer (32 GB ram, Intel Core i7 @ 3.6 GHz) used for this project and with the settings chosen (detector resolution, number of rays, and MCP input/output plane resolution) each channel took about one minute to simulate. When simulating the short trajectories 721 holes were needed to cover the

entire area of the MCP input plane that was hit by light. For the long trajectories 1261 holes were needed. A simulation hence took about 12 or 21 hours to complete, depending on if it was a long or short trajectory simulation. In total 12 simulations were performed, divided between long and short trajectory (5 and 20 mrad divergence), near field and far field, and 29, 41, and 69 nm wavelength. Near field simulations were performed by inserting a focusing lens in the beamline after the MCP. Simulations were also made without an MCP in the system, for comparison. The results of the simulations can be found in section 4.1 and in the appendix. The wavelengths used were chosen to correspond to the wavelengths of harmonic 35, 25, and 15 of a 1030 nm wavelength driving laser. In figure 9 the result of a typical far field simulation can be seen.

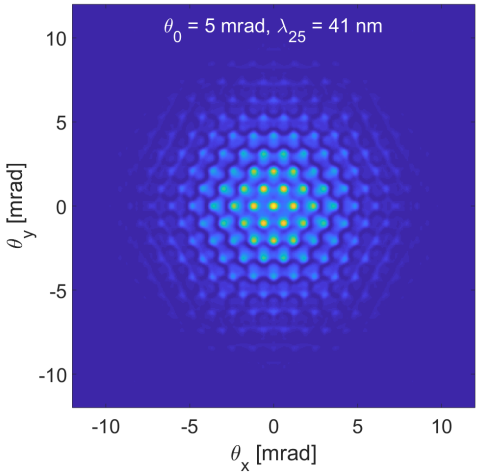

Figure 9: A typical result of an MCP simulation using FRED.

3.1.1 Testing the method

To test if the method gives somewhat reasonable results a simulation on a system with an analytically known solution was performed. The test was done with only the input plane; resynthesizing the rays only once, thus simulating thin optics. The distance to the detector was the same as for the simulations described in the above section.

Only one circular hole was used and the light source was replaced by a collimated Gaussian laser beam. The analytically expected outcome of this is that the first intensity minima should be found at the angles

$$\theta \approx \pm 1.22 \frac{\lambda}{d} \approx 8.4\,\text{mrad},$$

where $\lambda = 69$ nm is the wavelength used, and $d = 10\,\mu$m is the diameter of the hole [17, p. 123].

The obtained intensity profile can be seen in figure 10. The first maxima are found at ± 4.94 mm, which corresponds to the angles $\theta = \pm 8.2$ mrad. Also, the pattern is the expected Airy pattern, seen when shining coherent light through a circular hole.

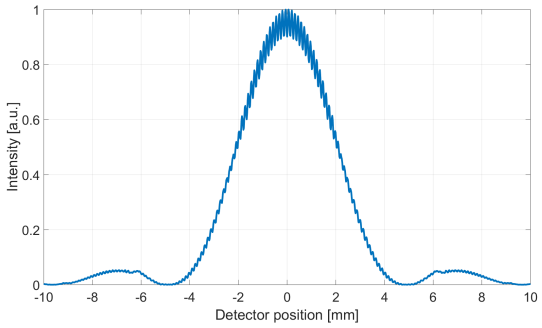

Figure 10: Obtained intensity profile using only one circular hole.

For one hole only, the method gives a result that agrees fairly well with the corresponding theory, which has been tested in numerous experiments. Hence, the method can be expected to give results that are physically relevant when used with multiple holes as well. This conclusion can be made since the full simulations of an MCP is made up of simulations of the individual holes, with the detected intensity profile being the sum of the light emerging from each hole.

3.2 Measuring the MCP divergence and transmittance in the visible regime

Using a very simple setup with an initially collimated beam, the divergence after passing an MCP and the transmittance through an MCP were measured. The setup consisted of a low power (<5 mW) continuous laser, two mirrors to change the direction of the beam, a lens to collimate the beam, an MCP, and either a screen (consisting of a checkered paper) or a power meter. The hole diameter of the MCP was 5 μm and the hole distance (center to center) was 6 μm, giving a hole to plate ratio of approximately 63%. The thickness of the MCP was 300 μm, giving a plate thickness to hole diameter of 60:1. After collimation the beam diameter was approximately 5 mm.

To measure the divergence, a screen was placed approximately 70 cm in from the MCP and the centers of the first order diffraction spots were marked. Figure 11 shows the diffraction pattern that was seen on the screen for the blue (405 nm) laser. The diffraction patterns for red (641 nm) and green (516 nm) were similar, but with different divergences. In the center is the bright zeroth order diffraction spot, and around it are diffraction spots of increasing order. The distance to the screen, as well as the distance between spots, were measured with a ruler and the divergence calculated as the average angle between opposite first order spots, i.e.,

$$\theta_1 = \frac{1}{3}\sum_{i=1}^{3} \operatorname{atan}\left(\frac{d_i}{z}\right),$$

where θ_1 is the first order diffraction spot angle, d_i is the distance between the i'th diffraction spot pair, and z is the distance between the screen and the MCP.

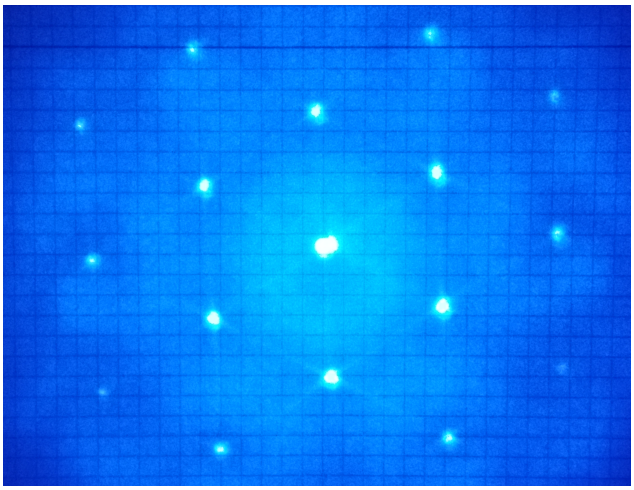

Figure 11: The resulting diffraction pattern when sending collimated blue (405 nm) laser light through an MCP.

The transmittance was measured using an optical power and energy meter, called PM110D, from Thorlabs. It offers the possibility to measure power with sub-microwatt precision in the visible to infrared (IR) part of the spectrum. However, when doing the measurements on the transmitted beam the uncertainties were much larger than this, as a consequence of the extremely high sensitivity in the transmittance to the incidence angle of the beam. An ever so slight deviation from zero incidence angle decreases the transmittance significantly. This is of course expected, since the channels are 60 times longer than their diameter, and hence the perceived opening area decreases rapidly when seen from an increasing angle. The total power of the unfiltered laser, P_{tot} and the power in the zeroth order diffraction spot, P_0, were measured. From the obtained values the transmittance was calculated as

$$T = \frac{P_0}{P_{tot}}.$$

This was repeated for the three available lasers (405 nm, 516 nm, and 641 nm) and the result can be found in figure 31, together with the measured divergences.

3.3 Characterizing the XUV wavefront

The wavefront of a beam consists of all adjacent points with equal phase. At any point in space the beam will travel in the direction that is normal to the wavefront in that point, and hence the beam will diverge or converge depending on whether the wavefront is convex or concave.

The direction of the wavefront in a particular point can be probed by propagating the beam towards a beam block with a small hole in it. The part of the beam that passes through the hole will continue in the direction that is normal to the wavefront of that part, and can eventually be recorded as a spot on a screen. The wavefront normal in the part that passed the hole can then be found by comparing the position of the spot with the corresponding position a flat wavefront would produce. By making several holes in a

grid pattern in the beam block and record the spots on the screen that each hole gives rise to, the entire wavefront over the grid pattern can be reconstructed. The accuracy of the reconstruction increases with a finer grid pattern, but if the holes are too close to each other it is not possible to distinguish which spot belongs to which hole and reconstruction becomes impossible. The holes must be small enough, so that the wavefront can be considered locally flat over their extent.

In figure 12 a wavefront incident on a Hartmann mask (Aperture array, in the figure) and the spot pattern recorded by an X-ray charge-coupled device (CCD) is shown. The green spots are the result of the measured wavefront and the white spots are the flat wavefront reference.

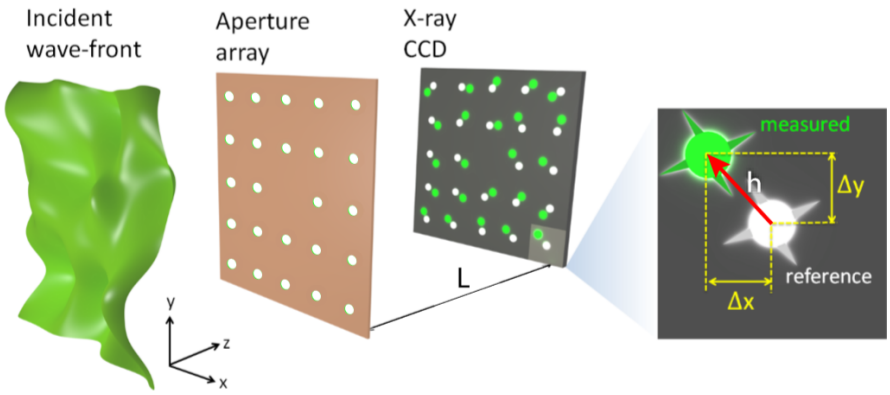

Figure 12: A sketch showing the basic principle of how a Hartmann sensor works. From [21].

The reconstruction of the wavefront is done by numerically finding the combination of, so called, Zernike polynomials that best reproduce the recorded spot pattern. Each of the Zernike polynomials is associated with an aberration, which for the lowest orders represent: tilt, astigmatism, defocus and coma. The error between the recorded pattern and the reconstruction decreases as the order of the polynomials is allowed to increase. The reconstructed wavefront can either be presented as a surface or as the coefficients of the Zernike polynomials.

The type of device that is described above is called a Hartmann sensor after its inventor, German physicist Johannes Franz Hartmann. In the Master thesis by F Brunner a sensor of this type, and a software to use it with, was constructed and proved to work [21].

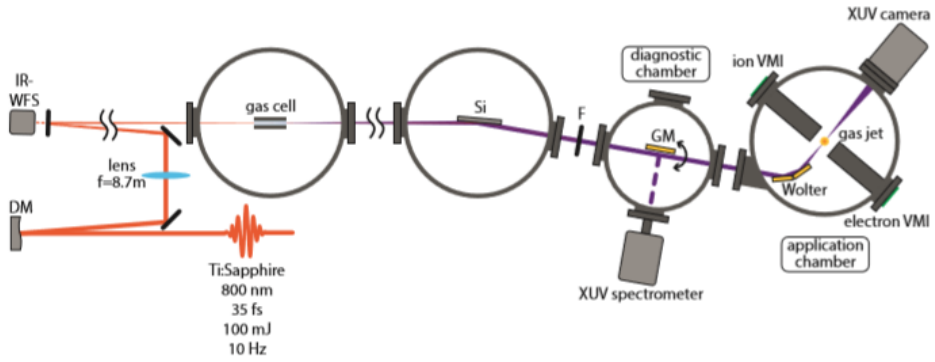

Figure 13: A schematic drawing of the intense XUV beamline used to characterize the wavefronts of XUV light passing an MCP. From [21].

The same sensor that was constructed by Brunner was used to measure the wavefront of XUV light that had passed through an MCP. The mask in the sensor is made from a 50 μm thick stainless steel plate and has 61 x 61 holes in it. The holes are placed in a square pattern 145 μm apart and have a diameter of 66 μm. It was placed in the diagnostic chamber of the intense XUV beamline sketched in figure 13. As its light source the setup has a 800 nm wavelength Ti:Sapphire laser, which is capable of producing 35 fs pulses at a rate of 10 Hz. The low repetition rate allows for single shot acquisitions.

Ca 1.5 m before the sensor a 40 μm thick MCP plate with 10 μm holes, giving a plate thickness to hole diameter ratio of 40:1, was placed on a translation stage. The translation stage allows the MCP to be moved in an out of the beam path when doing measurements. A stationary aluminum filter was installed before the MCP to remove the IR, while (partly) letting the XUV through. The MCP was aligned by rotating it to maximize the throughput, monitored by a power meter.

Before starting the measurements the beam was aligned to minimize aberrations. Several acquisitions, each consisting of a single laser shots, both with and without the MCP, were made. In the end 70 with and 74 without the MCP could be used for analysis. The result of the analysis is shown in figure 32 in section 4.3.

3.4 Scanning the chirp of the driving laser

As described in section 2.2.3 the relative phase of the long and short trajectories will depend on the intensity, or amplitude, of the driving IR field. To gain greater insight of this relation it has to be probed experimentally. This can be done by scanning the driving laser intensity directly, i.e., by attenuating the laser. Doing this one will be able to measure how the intensity of the generated XUV fluctuates, due to interference between long and short trajectory contributions.

When doing chirp scans, i.e., scanning the driving laser intensity by changing the pulse duration, the setup in figure 14 was used. It consists of an industrial graded turnkey PHAROS laser from Light Conversion, optical components to align and redirect the beam (not shown in the figure), a 100 mm focusing lens on a

longitudinal translation stage, a generation chamber with a 50 μm gas nozzle on a 3D translation stage, a differential pumping section with pinholes in each end to restrict gas flow, and a detection chamber with a focusing grating and an MCP screen. A high flux roughing pump is connected to the generation chamber to pump out gas injected through the gas nozzle. The two turbo pumps, which are connected to the differential pumping section and detection chamber, respectively, have a common backing pressure, supplied by another roughing pump. In the detection chamber the generated harmonics are separated according to wavelength and focused on an MCP screen by a grating. The MCP screen is recorded by a CCD camera.

The overall dimensions and angles of the setup are set by the grating. Unfortunately there is a flaw in the design. The angle that the central line of the generation chamber and differential pumping section makes with the cone holding the MCP screen, is approximately 4° to small. To compensate for this the second pinhole is offset to the right (looking along the beam), allowing the beam to reach the grating with an angle more similar to the intended angle. This, in turn, means that the MCP screen is not perfectly aligned with the grating, giving a worse focus than ideal.

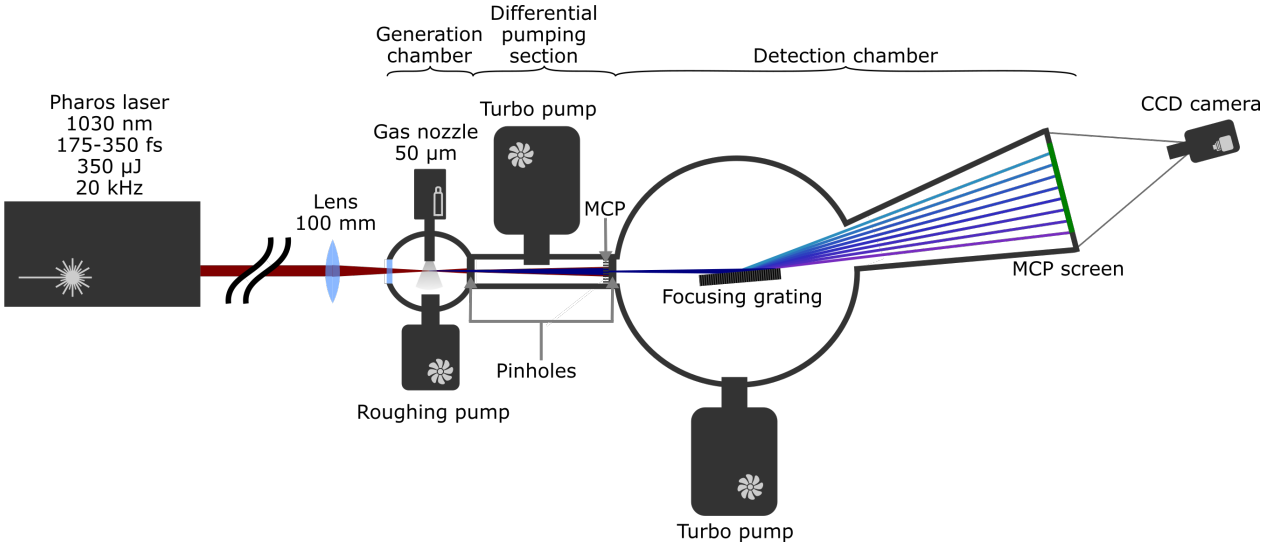

Figure 14: A schematic drawing of the setup used for the chirp scans. The laser specifications are those used in the experiments.

The laser in the setup allows the chirp of the pulses to be changed by stepping a compressor. This means that scans can be performed where the chirp, and hence the pulse duration and peak intensity, is changed in small steps, while each resulting spectrum is recorded by the CCD camera. As explained in section 2.2.3, a change in peak intensity will lead to a change in the phase difference between long and short trajectory contributions; see specifically equation 7. This can be seen as local fluctuations in intensity in areas where long and short trajectory overlap spatially, and hence interfere. By choosing to look at just one harmonic at the time and putting the central one pixel columns of that harmonic next to each other, as the compressor is stepped, a new image with compressor position on the x axis and the spatial divergence on the y axis is formed. The way such a picture is formed is illustrated in figure 15, where spectra with increasing chirp is

lined up after each other and "cut" along the dashed white lines to obtain the QPI plot in figure 16a. Doing this allows the QPI to be clearly seen as fringes, i.e., a modulation of the overall intensity. The fringes are a result of interference between the two trajectory contributions, and can therefore provide information about the α's in equation 6 and 7.

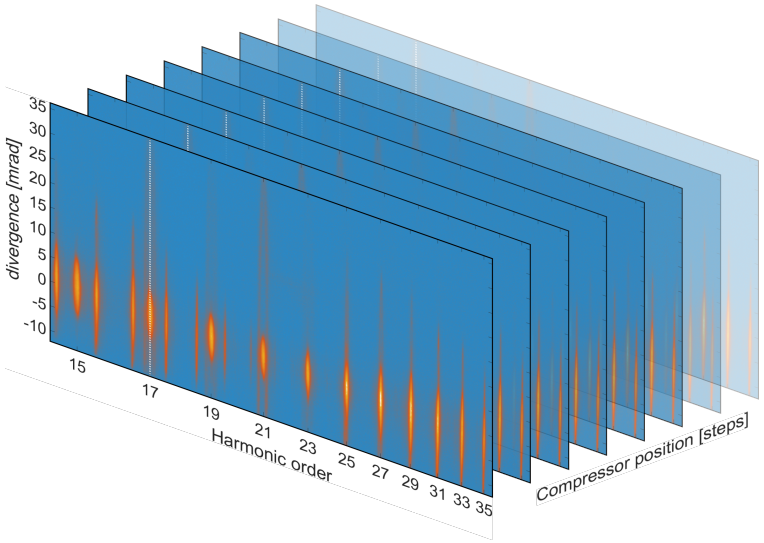

Figure 15: The chirp scan spectra are being cut along the dashed white line to be able to see QPI.

The QPI plot has compressor position on the x axis, which is what is actually changed between consecutive acquisitions, but it is not a physically relevant variable. It would be better to use pulse duration, but to go from compressor position to pulse duration is not straight forward, since the pulse duration is hyperbolically dependent on the compressor position, and the mapping from compressor position to duration is different for each individual laser. However, close to the minimum pulse duration this relation can be approximated by a (mathematically simpler) parabola. A parabolic relation between pulse duration and compressor position has already been found by fitting the code described in section 2.3 to the result of earlier chirp scans [10]. The easier route would be to just change the scale on the x axis according to that quadratic function, but that would give a non-linear x axis. Instead the QPI plot was interpolated, using the Matlab function `interp1`, according to the parabolic compressor position – pulse duration mapping and a desired linear set of pulse durations. The result of this interpolation process is displayed in figure 16b. As seen this QPI plot is more compressed in the central parts than the plot in figure 16a. This is due to the pulse duration barely changing when the compressor is moved close to its central position. One might note that the minimum pulse duration does not coincide with the highest intensity, as expected. This is due to the intensity of all harmonics being used when finding the central compressor position, not just harmonic 17.

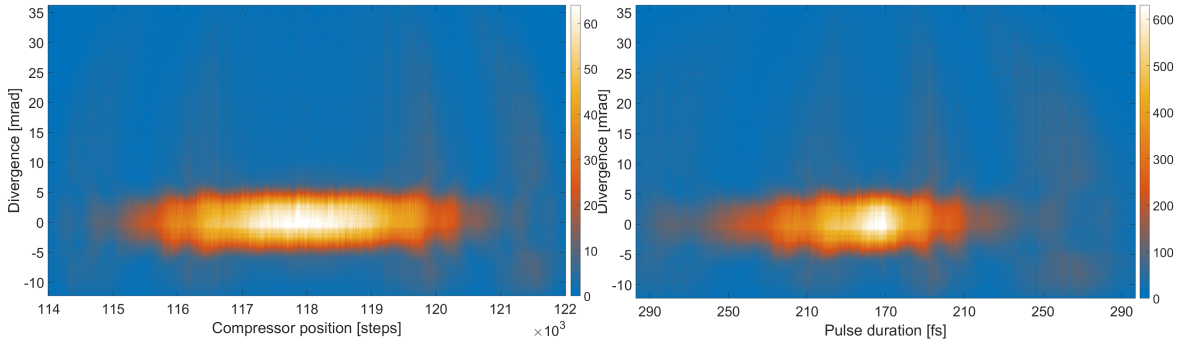

(a) The 2D harmonic 17 QPI plot, cut from the 3D chirp scan data in figure 15.

(b) The exact same data as in figure 16a, but interpolated to have linear pulse duration on the x axis.

Figure 16: The same QPI plot, but with different x axes.

Another thing to take note of is that even though the x axis is linear everywhere it has a discontinuity at minimum pulse duration, where the slope changes sign from negative to positive. This means that in a full chirp scan each intensity is scanned twice, with the sign of the chirp being the opposite the second time.

A positive chirp means that the higher frequencies are trailing, while the opposite is true for a negative chirp [22]. It is not obvious that this difference in chirp should affect the way harmonics are generated, and if it does not, the left and right halves of the QPI plots should be mirrored around the shortest pulse duration.

The part of the plot in figure 16b where long and short trajectory emissions overlap, i.e., approximately between plus and minus 5 mrad, consists of three components: (1) a low amplitude random noise, (2) an overall intensity that is highest close to the minimum pulse duration, and (3) smooth oscillations, seen as fringes, due to QPI between long and short trajectory contributions. In these experiments the third component is the one of interest, since it is the only component that carries information about the phase accumulation associated with long and short trajectory, respectively. To get rid of the other two components the data is first subject to an ideal low pass filter, with the result presented in figure 17a, and second to a filter that removes a moving average of each row, with the result presented in figure 17b. After applying these filters the plot is said to be contrast filtered, i.e., filtered for maximum contrast of the QPI. The result is a QPI plot with linear pulse duration on the x axis and high visibility of QPI. It is worth noting that filtering also makes structures off-axis - where it is assumed that only long trajectory is present - much more visible.

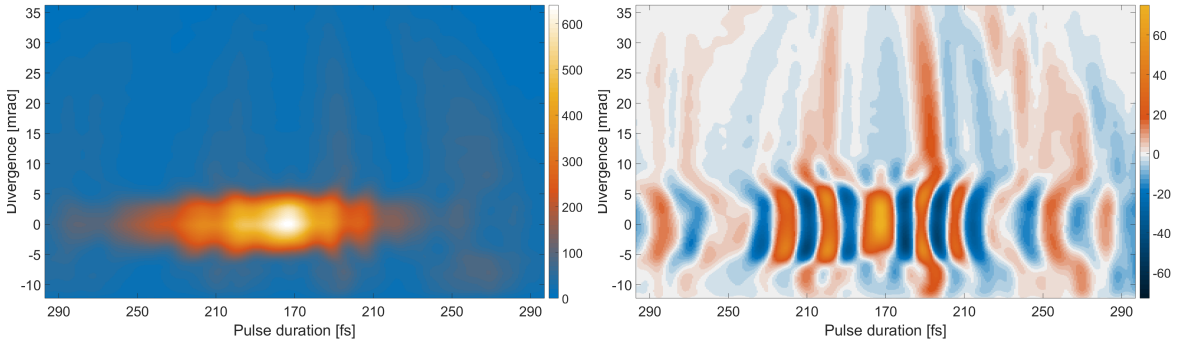

(a) Low pass filtered. **(b)** Contrast filtered.

Figure 17: The same QPI plot, but with different levels of filtering applied.

In figure 18 the zero divergence rows of figure 16b and 17 are plotted together with the moving average that was subtracted to obtain the contrast filtered curve. These curves will further on be called lineouts. Actually, the raw data lineout was obtained by just monitoring the intensity of the central pixel of harmonic 17, as the pulse duration was scanned. The big central peak of the contrast filtered lineout is an effect of the filtering process and should not be considered further.

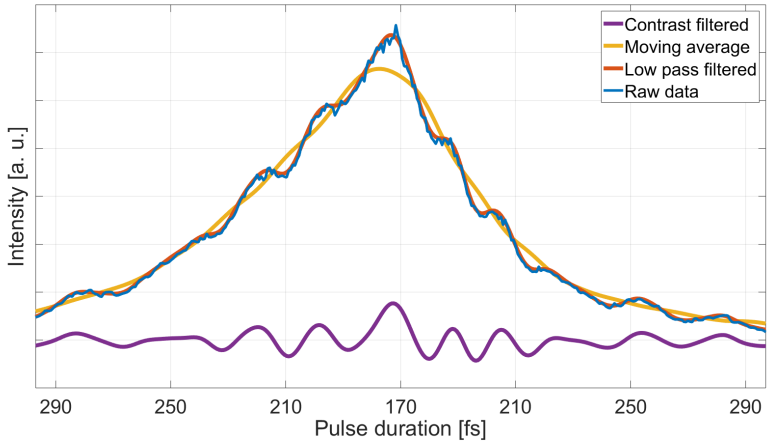

Figure 18: On axis lineouts from figures 16b and 17.

3.4.1 Two dimensional chirp scans

In addition to scanning the chirp dimension, a second dimension can be scanned by changing another parameter between consecutive chirp scans, thus making the scan two dimensional (2D). The other parameter can, for example, be laser attenuation (decreasing the overall power), laser polarization or position of the laser focus. If this other parameter also has an effect on the phase difference between long and short trajectory contributions the position of fringes will move as this parameter is varied. In this project two 2D scans were made: one chirp – focus with 29 focal positions in steps of 100 μm and one chirp – attenuation in 15 steps

of 1 percentage point (70 mW, which is 1% of the maximum power). In both cases the chirp was scanned in 401 compressor steps from 114000 to 122000, thus making the step size 20.

The chirp – focus scan was made to see where the lens should be placed to get the best contrast for QPI between long and short trajectory. As it turned out the scan also made it possible to find the position of the center of the gas jet, relative to the focal point. After performing these scans the data was filtered as described above and the lineouts for every focal position were put on top of each other to form a - from here on called - lineout stack, exemplified in figure 19. This was done for every harmonic, and for every harmonic the positions of the fringes that were clearly visible were traced. The tracing was done semi-automatically with a short code developed during the project. The code requires the user to graphically input the desired starting and ending position of each fringe, hence it is not fully automatic. It would be difficult to make the code itself determine these starting and ending positions, since it is sometimes hard to see in what interval a fringe can be traced with confidence. A quadratic function was finally fitted to each trace. The fringes, traced positions and fitted curves can be seen in figure 19.

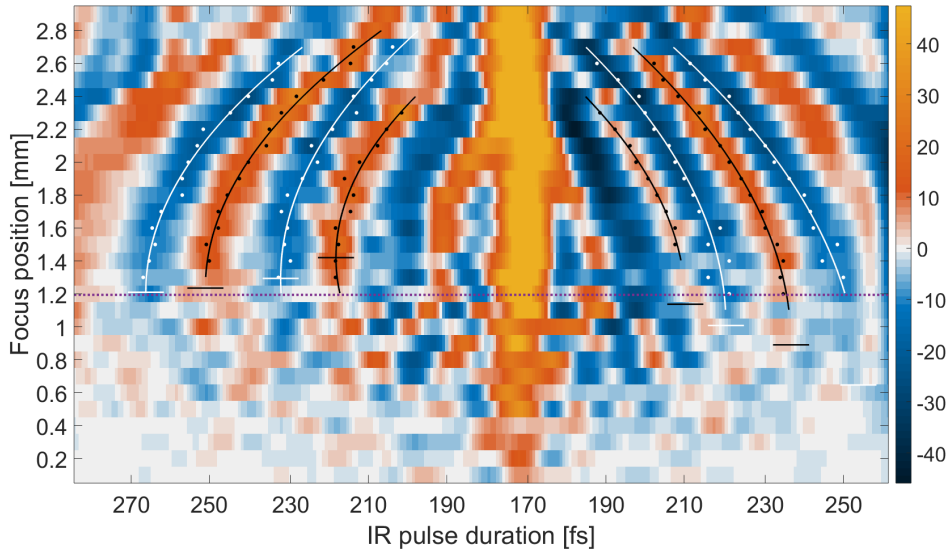

Figure 19: A lineout stack with traced fringes for harmonic 19, from a chirp – focus scan. The white (black) dots are positions of local intensity minima (maxima), the curved lines are fitted quadratic functions, the horizontal short lines mark the extreme points of each quadratic functions, and the dotted purple line is the average of all the extreme points.

Drawing from the chirp-focus scan it was assumed that the center of the gas cell is located at the average extreme point of the curves in figure 19. The lens was then placed so the focus ended up 0.50 mm after the center of the gas cell, where it seemed to give the best QPI contrast. With the lens in this position a chirp – attenuation scan was performed. After scanning nine attenuations the entire setup was shut down, meaning that the laser was turned off, the gas supply closed and the voltage over the MCP screen removed. The scan was resumed the day after with the same settings, for another six attenuations. This break in the scan is marked in the results with a dotted white line. An example of a resulting lineout stack can be seen in figure

20, which is similar to what is seen in figure 19, but with linear fringe movement.

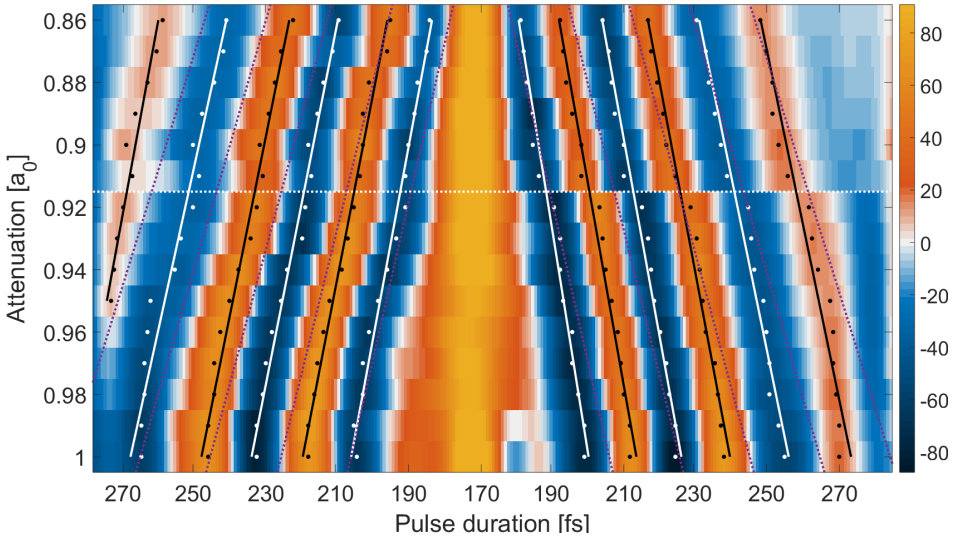

Figure 20: A lineout stack with traced fringes for harmonic 17, from a chirp – attenuation scan. The white (black) dots are positions of local minima (maxima), the lines are fitted linear functions and the purple dotted lines represent the expected slopes of those lines. The white dotted line marks the end of the first day of the campaign.

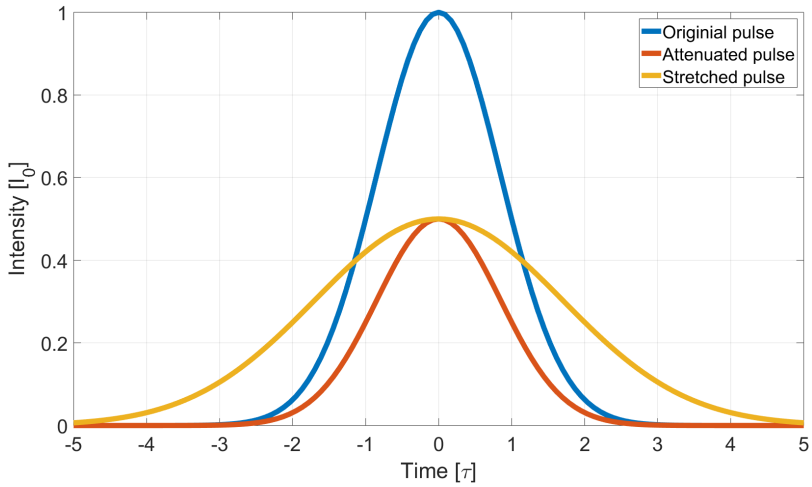

Figure 21: The peak intensity of the original pulse (blue) has been decreased by either stretching (red) or attenuating (yellow) it.

The assumption, when doing a chirp scan, is that it is effectively an intensity scan, i.e., that the IR peak intensity is the only contributor to the phase difference between long and short trajectory. To either change the chirp or to change the attenuation of the laser, will affect the IR peak intensity, but in slightly different ways. The assumption is that the effect of the different ways is negligible. Changing the chirp will stretch (compress) the pulse, and hence indirectly lower (raise) the peak intensity, but keeping the pulse energy constant. In contrast, attenuating the pulse will directly decrease the peak intensity, while keeping the pulse

duration constant. In figure 21 the effect of attenuating and stretching a pulse is shown. When stretching the pulse the area under the graph (yellow) remains the same as for the original pulse (blue). If the assumption that stretching and attenuating has the same effect on HHG holds, then the fringe movement seen in the lineout stack can be predicted. This is because being at a certain position (e.g. a maximum or a minimum) of a fringe means that the phase difference of long and short trajectory has a certain specific value. When that position of the fringe is traced through the 2D scan, one actually traces a line where the phase difference between long and short is constant. If now peak intensity is the parameter that is most relevant for phase accumulation (see equation 5-10), this is also a line where the peak intensity is approximately constant. Hence we know that

$$I_0(\tau, a) \propto \frac{1}{\tau} a \approx constant, \tag{12}$$

where τ is the pulse duration, controlled by changing the chirp, and a is the attenuation, along this line. This means that the observed fringe traces can be compared with lines where equation 12 holds exactly, to evaluate whether or not the assumption that a chirp scan is in effect an attenuation scan is correct.

The advantage of a chirp scan over an intensity scan is a longer scan range with good signal. This can be seen in figure 20. A vertical lineout, across the attenuation axis, would only cut through one half oscillation, making it hard to accurately determine how the phase difference of long and short trajectory emissions depends on the intensity. On the other hand, a horizontal lineout from one side to the center - i.e., a cut across chirp - could cut up to three oscillations, giving a derivation of the intensity – phase difference relation much more statistical power. Cutting from one side all the way to the other would not add much, since it is assumed to be the same as doing the same scan twice, hence three oscillations, and not six, in the comparison. In the figure it appears as if one could continue decreasing a, the attenuation factor, a bit more, but the signal is actually starting to become too weak, where the scan was stopped (at 14 % attenuation, i.e., $a = 0.86a_0$).

The resulting stacked lineouts of harmonics 15 to 31 for this scan are found in figure 35 and the absolute values of the slopes are plotted in figure 36.

3.4.2 Chirp scan with an MCP filter

The main goal of this project is to evaluate whether or not an MCP can be inserted in an HHG beamline without interfering with the phase - and hence curvature - of the generated wavefronts. To do this two chirp scan from compressor position 114000 to 123000 in 451 steps were performed with and without an MCP in the beam line. The lens was placed to get the IR focus 50 μm after the center of the gas jet. The scan without the MCP was done first and after that the chamber had to be opened and an MCP inserted at the position indicated in figure 14. The plate with offset pinhole, described in the beginning of section 3.4, was left in the setup as the MCP was inserted. This could have been problematic, since the offset pinhole requires the beam to come in with a slight angle, while the transmission of the MCP is very sensitive to deviations

from normal incidence, but the XUV spectrum could still be detected. The particular MCP that was used had a thickness off 400 μm and a hole diameter of 10 μm, making the thickness to hole ratio 40:1. Therefore it was not possible for a beam to pass directly through the MCP, i.e., without reflecting in the channels, if the incidence angle was larger than atan(1/40) $\approx 1.4°$.

After installing the MCP some realignment had to be done, but the position of the lens was left unchanged, hoping that the focus would remain in the same position, relative to the gas jet, as before. The resulting spectra are displayed in figure 22. In figure 23 is a zoom in on the MCP spectrum, showing harmonic 15.

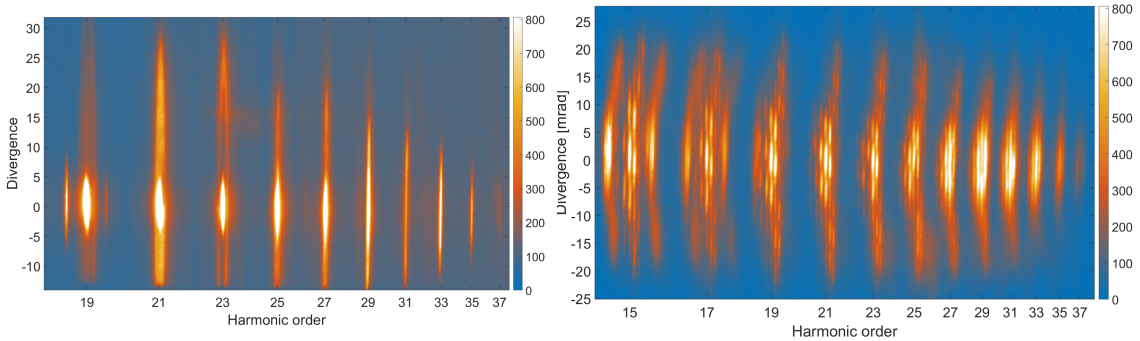

(a) Spectrum without MCP.

(b) Spectrum with MCP.

Figure 22: Two spectra, acquired with and without an MCP in the beamline.

The distance from the center to the first order diffraction spots, numbered from 1 to 6 in figure 23, was measured by marking - what was perceived as being - the center of each spot 5 times. The radial divergence for each spot and harmonic order was calculated and plotted in figure 42.

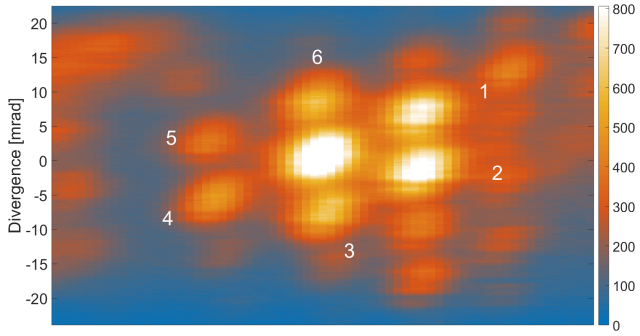

Figure 23: A zoom in of figure 24b, showing harmonic 15.

The QPI plots of harmonic 15 to 31 were contrast filtered for both scans, and in figure 24 the plots for harmonic 19 are shown.

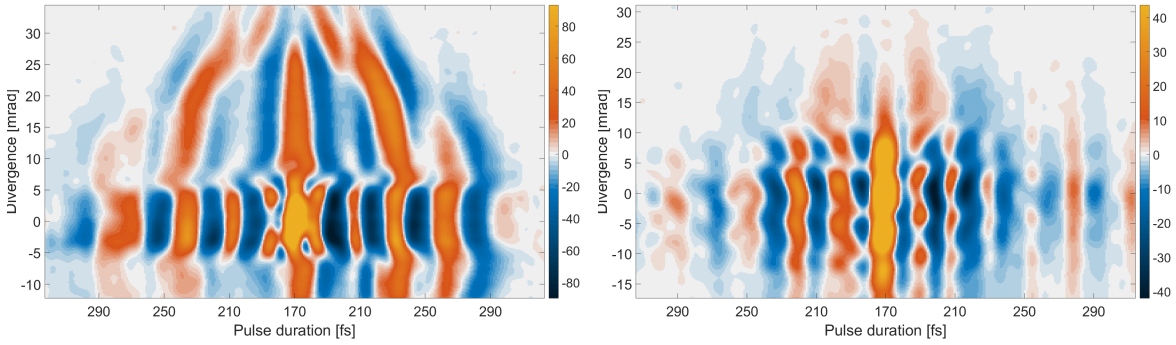

(a) QPI plot without MCP. **(b)** QPI plot with MCP.

Figure 24: Two plots of harmonic 19, acquired with and without an MCP in the beamline.

As seen in figures above, the spectra and QPI plots obtained with an MCP in the setup has a lot of unwanted modulation, but it might still be that the central part is unaffected by the MCP. Therefore the part containing the central row ±5 mrad of the contrast filtered plots were plotted together, to make visual comparison easy. An example of this on-axis comparison is displayed in figure 25. The on-axis comparisons of the rest of the harmonics can be found in figure 41.

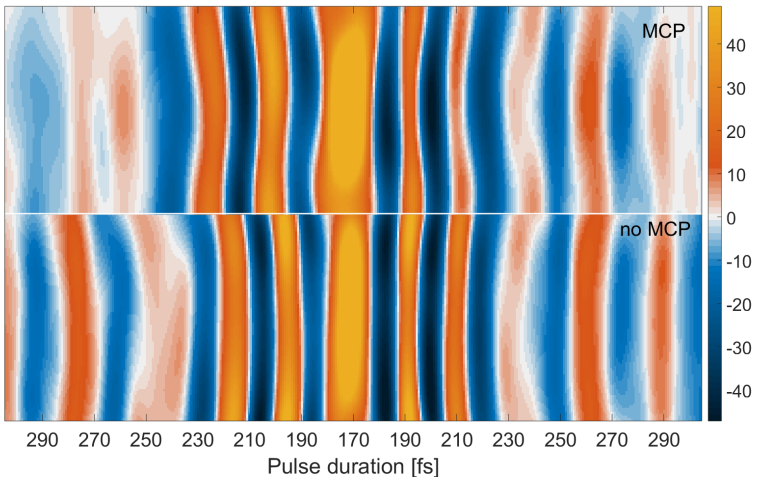

Figure 25: An on axis comparision of the contrast filtered QPI plots obtained with and without an MCP in the beamline for harmonic 17.

3.5 Possibly a third trajectory

In figure 26 contrast filtered QPI plots of harmonic 15 to 33 are shown. From harmonic 23 and upwards the plots do not only show on-axis oscillations along the pulse duration, but also more of an off-axis ring structure. This ring structure is itself modulated, so that if a ring is traced a variation in intensity is seen, making rings disappear both on- and off-axis.

The source of this modulation is not known, but it is not reasonable to think that it is the contributions

from short and long trajectories that interferes with each other, since in the off-axis region the short trajectory emission is not present. The natural assumption to make is that it is either interference within the long trajectory emission, or the long trajectory contribution interfering with a *longer* trajectory - i.e., a third trajectory - contribution.

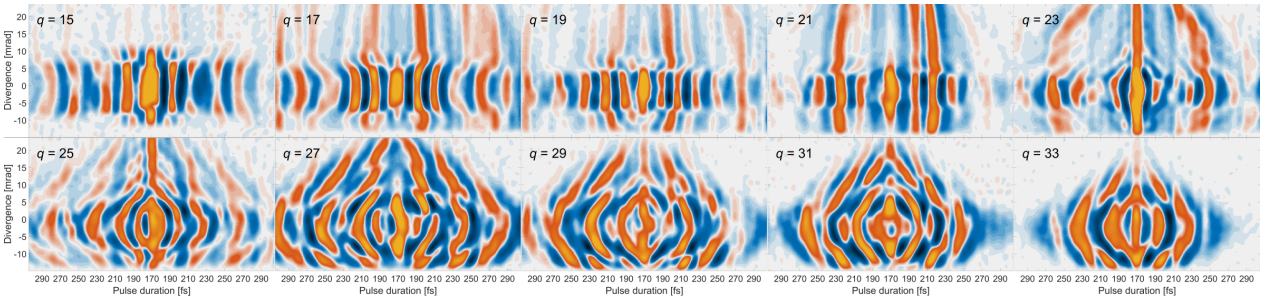

Figure 26: Contrast filtered QPI plot of harmonic 15 to 33.

To test if this could be an observation of the - previously unseen - third trajectory the code described in section 2.3 was used to simulate chirp scans. Harmonic 31 was chosen to represent the higher harmonics, due to it showing the observed ring modulation phenomenon particularly clearly, and the code was used to try to replicate its appearance. The best resemblance with the experimental QPI plot was sought by carefully adjusting N and the α's for long and short trajectory, starting from the values presented in [10]. When no better resemblance could be achieved, another wavefront - a third - was added and the process repeated.

In figure 43 the experimental data for harmonic 31 can be found together with simulations using two and three wavefronts, respectively.

3.6 Improvements on the setup

When starting the project the scans described in section 3.4 were performed by repeatedly (1) pressing a computer button to step the laser compressor, to change the chirp, and (2) pressing another button to acquire an image with the CCD camera. The acquired image is an average of a specified number of images. Therefore, with an acquisition rate of ca 20 fps and normally 100 images used, each acquisition took about 5 seconds to complete. Since the process was performed manually one person was supposed to click two buttons on a computer screen every five to six seconds for an hour or more. During this time it was crucial that no mistake was made, so that not, for example, an acquisition was made without first moving the compressor. On more than one occasion it might have happened that the author did miss clicking a button, rendering all the acquired data close to useless. During the entire scan the scanning person had to be in the lab and lights had to be on, for laser safety reasons.

Using existing LabVIEW code snippets, for establishing contact with the laser and moving its compressor, a scan program was updated to automatically perform the process described above. This opened up the possibility to do both finer and longer scans.

During one of these automatic scans it was discovered that the light shielding device - the light screen - which connects the MCP screen and the CCD camera while stopping outside light from reaching the camera, was insufficient. In figure 27a it is obvious that the background noise suddenly increases, due to somebody switching the lights on in the lab. To solve this problem a new light screen was custom sewn from a blackout curtain. The new screen is seen in figure 27b.

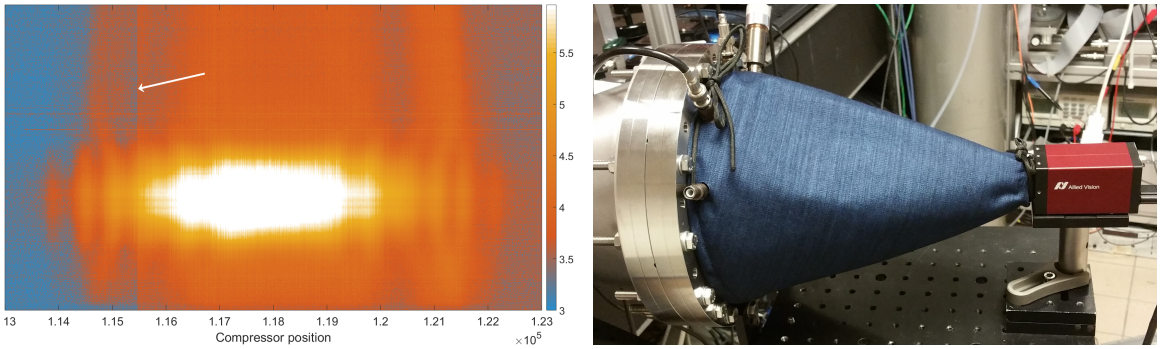

(a) The light was turned on at the arrow. **(b)** The new light screen.

Figure 27: The problem of external light leakage and it solution.

To test the new screen images were acquired with the ceiling lights on and off, for (1) no screen, (2) the old screen and (3) the new screen. The mean pixel values of these images were then compared. The lights off condition was not completely dark, since a computer screen was on and the door leaked some light. The result can be seen in figure 28. It shows that with the new screen it is not possible to distinguish between lights on and lights off, but it was with the old screen.

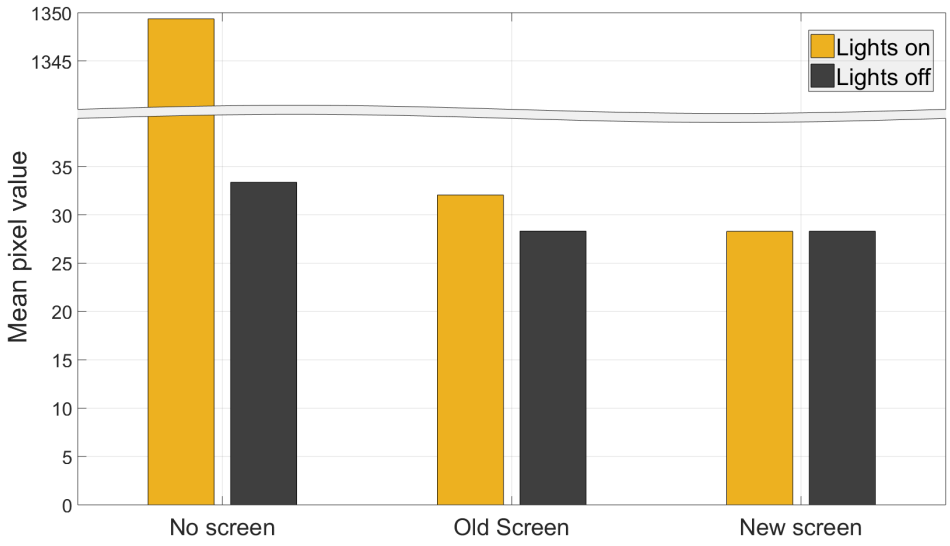

Figure 28: The result from testing different light screens.

The improvements described above are simple, yet they have a significant impact on the performance and utility of the experimental setup. At the time of writing both improvements have been used in other

campaigns, improving and simplifying data acquisition.

4 Results and discussion

In the following section the results of the experiments and simulations described in section 3 will be presented. The results that concerns XUV transmission through an MCP will be presented first, followed by the results that are related to the QPI scans, and finally the results of using an MCP filter in QPI experiments. The results will be discussed as they are presented.

4.1 FRED simulations of an MCP filter

The complete results from the MCP simulations includes all combinations of (1) far field or near field, (2) long trajectory or short trajectory, and (3) 29, 41 or 69 nm wavelength; in total 12 simulations. Here only the results from the 41 nm simulations are presented - in figure 29 and 30 - the others can be found in the Appendix. The corresponding figures in the Appendix show great similarities with figures 29 and 30 in this section, in that they also have a honeycomb pattern with an approximately Gaussian envelope in the far field and an almost perfectly Gaussian beam profile in the central part of the near field. In all cases a longer wavelength results in a more divergent far field beam and a wider near field focus. It should also be pointed out that the hexagonal symmetry, which results from the MCP hole pattern, remains visible even in the near field, and more so for longer wavelengths.

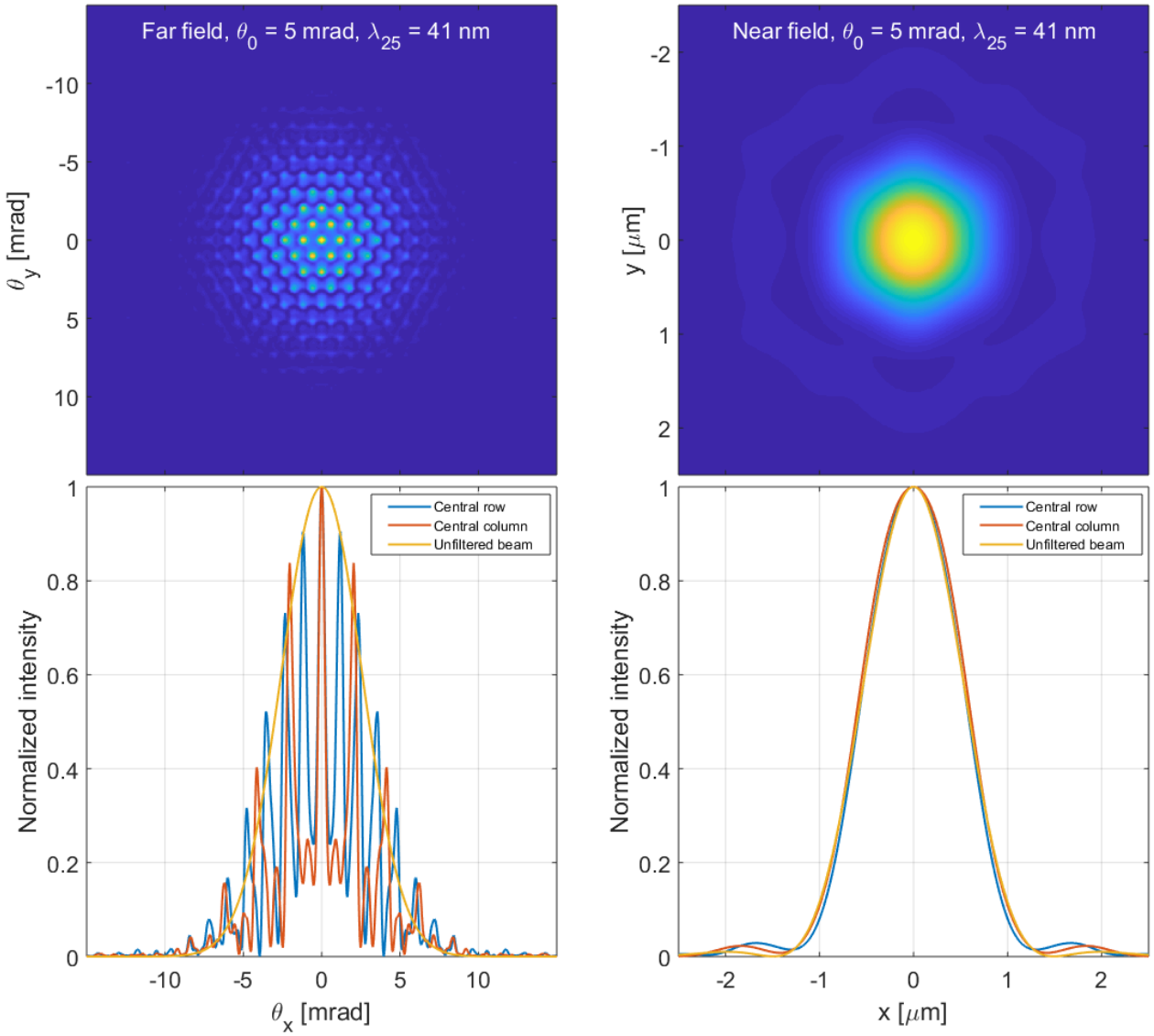

Figure 29: Simulated MCP diffraction patterns, resulting from a Gaussian laser beam with 5 mrad half width divergence and 41 nm wavelength. Left: The pattern seen in the far field with the central row and column plotted below. Right: The pattern seen in the near field with the central row and column plotted below. In the bottom plots the unfiltered Gaussian beam is added for reference.

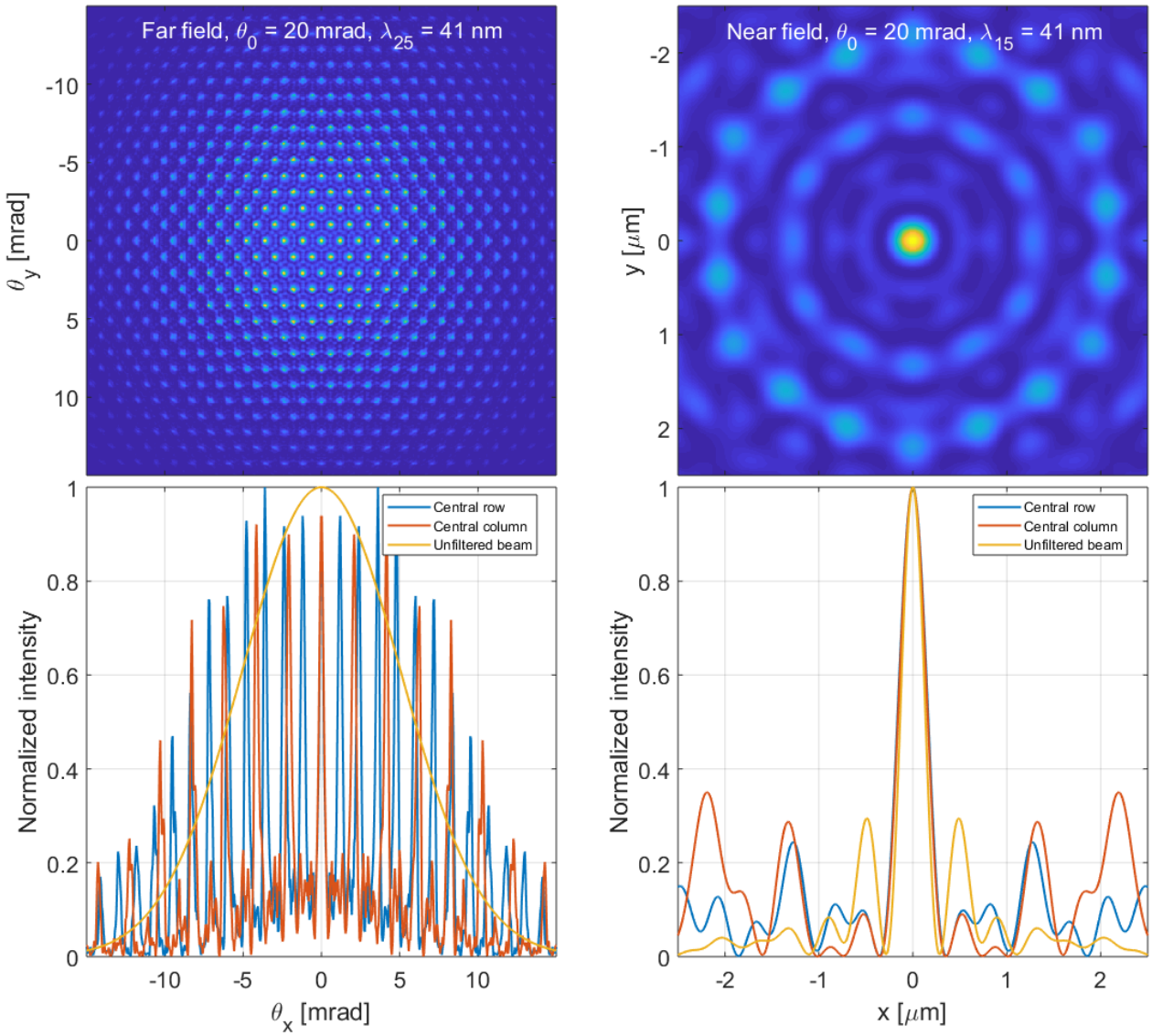

Figure 30: Simulated MCP diffraction patterns, resulting from a Gaussian laser beam with 20 mrad half width divergence and 41 nm wavelength. Left: The pattern seen in the far field with the central row and column plotted below. Right: The pattern seen in the near field with the central row and column plotted below. In the bottom plots the unfiltered Gaussian beam is added for reference.

These simulations are in no way conclusive, since the method has not been properly tested. The simple test in section 3.1.1 was in good agreement with theory of one hole diffraction, but does not necessarily translate to simulations of an MCP. For instance, the simulations does not consider reflections within the channels, even though that most likely occurs for XUV beams with gracing incidence angle. To include this phenomenon a completely different simulation technique is required.

Another problem is that it is not possible to tell which - if any - of the individual spots seen in the far field (left side of figures) should be considered as structures within the zeroth order (central) diffraction spot, and which should be considered higher order diffraction spots. If just the most central spot makes up the

zeroth order, then it is very small (ca 1 mrad) compared to what is seen experimentally (ca 5 mrad) in, for example, figure 23. The trend of the first order diffraction spot detection angle is expected to be increasing with increasing wavelength, but in these simulations it is non-existing. Despite this, the pattern do change with wavelength, so it is definitely an interference pattern and not just a projection of the MCP.

The near field patterns are very similar to what is seen with an unfiltered beam and, hence, look well behaved. This is most obvious for the short trajectory (5 mrad initial divergence) simulations, where the similarity of the MCP filtered beam and the unfiltered beam is almost perfect. This is in agreement with the successful near field MCP experiment in [7]. The trend of the focal spot size is also correct, with a smaller spot size for shorter wavelength.

4.2 MCP divergence and transmission in the visible regime

The transmission of the zeroth order (central) diffraction spot, as well as the divergence of the first order spots for collimated red (641 nm), green (516 nm), and blue (405 nm) lasers has been measured and the result of this is presented in figure 31.

The transmission measured is the transmission of the part of the beam that continues in the direction of the incoming beam, i.e., it is the intensity in the zeroth order diffraction spot divided by the intensity of the unfiltered beam. The uncertainties in these measurements are large, due to a high sensitivity in transmission to the angle between the MCP and the incoming beam. However, the trend of a transmission that decreases with increasing wavelength is clear. The decrease might be exponential.

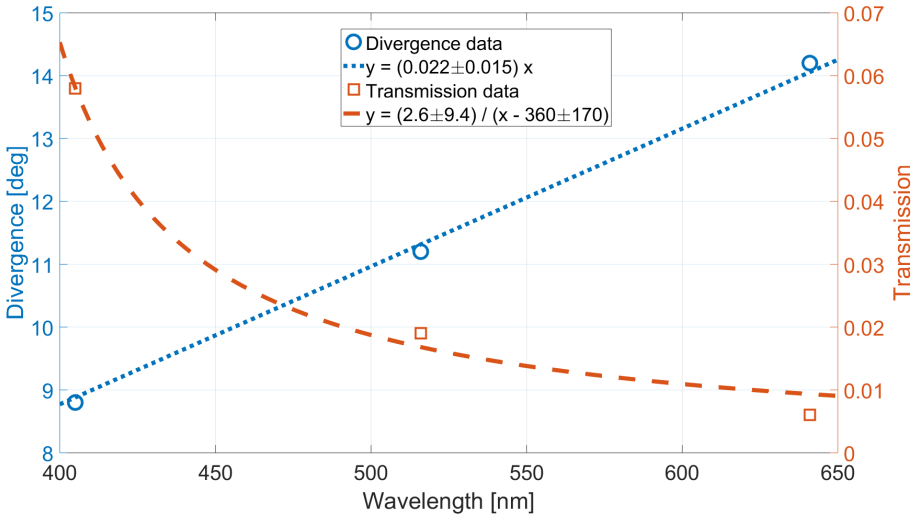

Figure 31: The measured divergence and transmission through an MCP with a plate thickness to hole diameter ratio of 60:1, a hole diameter of 5 μm and a hole spacing of 6 μm, giving a hole to plate ratio of 63%.

The divergence angle is the angle between the opposite first order diffraction spots. As seen it is increasing linearly with the wavelength. Extrapolating to the wavelength of harmonic 15 (69 nm) would give a divergence

of 26 ± 18 mrad, which does not seem to agree with what is seen in figure 42. However, the MCP's used in the two cases are different and therefore no proper comparison can be made.

The most obvious weakness with this experiment is the low number of data points, which was set by the number of different available low intensity lasers. If the experiment was to be performed with the laser in figure 14 in concert with an optical parametric amplifier (OPA), an arbitrary number of wavelengths from infrared to ultraviolet could be used.

4.3 Characterization of the XUV wavefront

The wavefronts of unfiltered and MCP filtered XUV pulses were characterized using a Hartmann sensor, as described in section 3.3. No difference between the two cases could be found. In figure 32 the values of the Zernike coefficients, used for characterization, are displayed. As seen, no coefficient has been altered by introducing an MCP in the beamline. The error bars are one standard deviation in each direction. Comparing blue (without MCP) rings to red (with MCP) error intervals (or vice versa), it is apparent that all the coefficients lay well within the interval that the corresponding error bars span. Therefore it can be stated that there is no difference between the wavefronts of unfiltered XUV pulses and the wavefronts of the zeroth order diffraction spot of MCP filtered pulses. Of course, this statement is only claimed to be valid to the degree of sensitivity the Hartmann sensor admits.

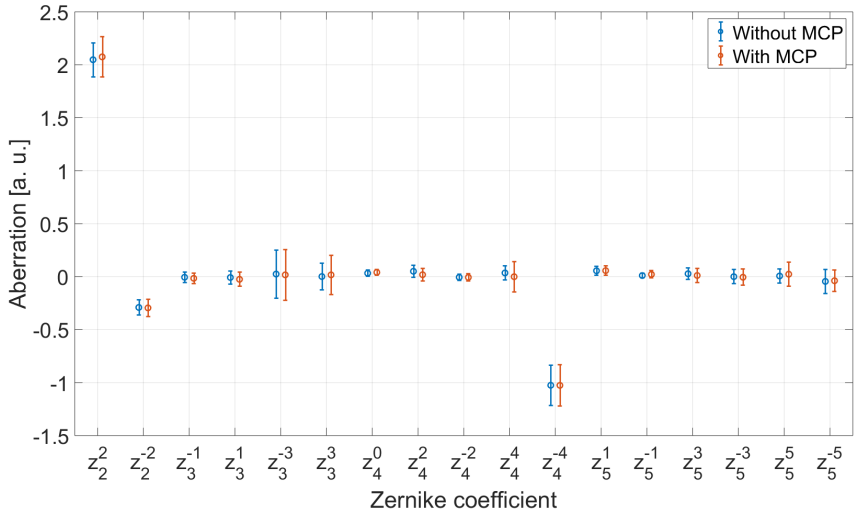

Figure 32: The values of the Zernike coefficients used to characterize the XUV pulse wavefront, with and without an MCP in the beamline.

4.4 Chirp scans

The results from the chirp scans will be displayed and discussed in the following sections. In the Method the 2D scans were in the same subsection, but here they have been separated for clarity. Also, some of the results

suggest that the analysis is repeated with different parameters. In those cases that process is described here, instead of in the Method, since previous results are needed to explain why things are done as they are.

4.4.1 Chirp – focus scan

The chirp – focus scan was mainly done to find the lens position that results in the best QPI contrast between long and short trajectory contributions. From figure 33 it is clear that good contrast is achieved as soon as the focal plane is moved a few 100 μm beyond the focal position called zero. It is also clear that it is the lower harmonics (from 15 to 19) that has the best contrast and, hence, the fringes that are easiest to trace.

It cannot be excluded that the chirp of the driving laser pulse affects the phase of the generated XUV light, but despite that the stacked lineouts in figure 33, all have an apparent symmetry. Both for lower order harmonics, with nice traceable fringes, and for higher order harmonics, with a noisier expression, the left (negative chirp) and right (positive chirp) halves look like reflections of each other. This indicates that the chirp of the driving pulse does not significantly alter the generation process, and that chirp scans can be used as intensity scans.

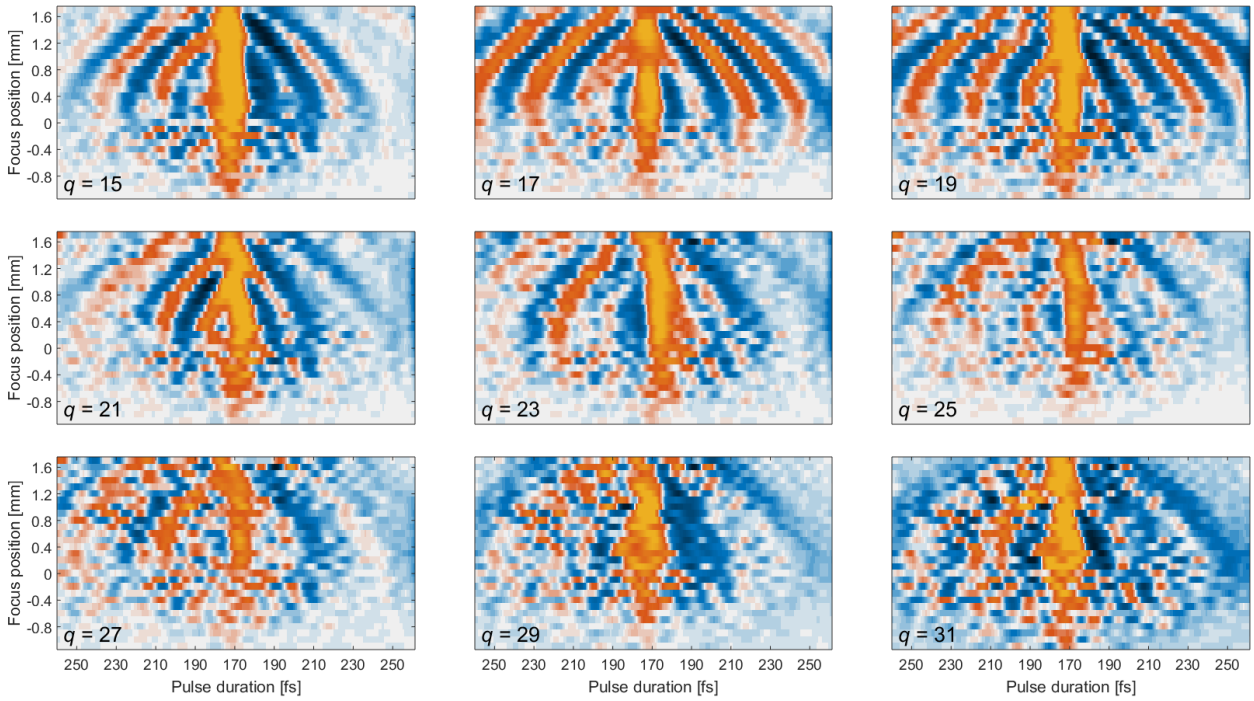

Figure 33: Stacked lineouts from the chirp-focus scan. The y axes has been adjusted to have zero at the average fringe extreme point.

When doing a chirp – focus scan the focal position of the driving laser is shifted along the optical axis. In this particular scan it was shifted from before the gas jet to after it. At some point during this scan the focus must have been centered on the gas jet, achieving the geometric situation with maximum intensity at the gas jet. In this situation each fringe is at its maximum pulse duration. These fringe extreme positions

were found by fitting a quadratic function to the traceable fringes in the stacked lineouts. In total there were 31 fringes, distributed over harmonic 15 to 25, which could be traced and associated with an extreme point. The position of these extreme points are plotted as functions of harmonic order in figure 34 together with their average value.

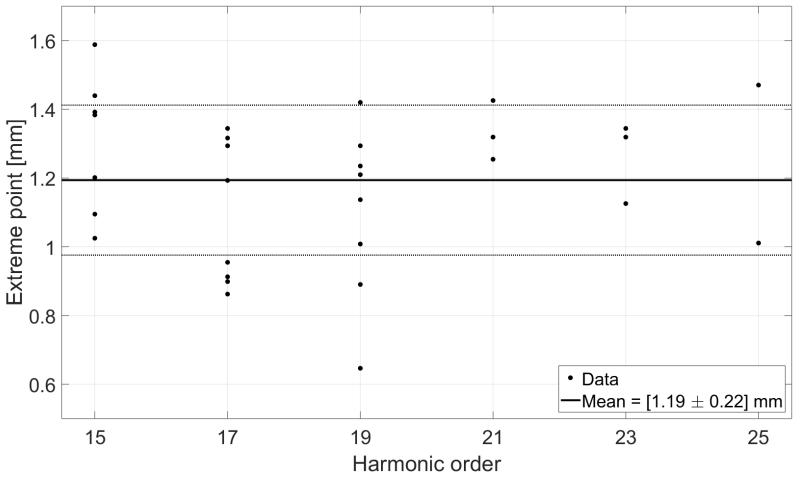

Figure 34: The extreme points of the traceable fringes in figure 33

4.4.2 Chirp – attenuation scan

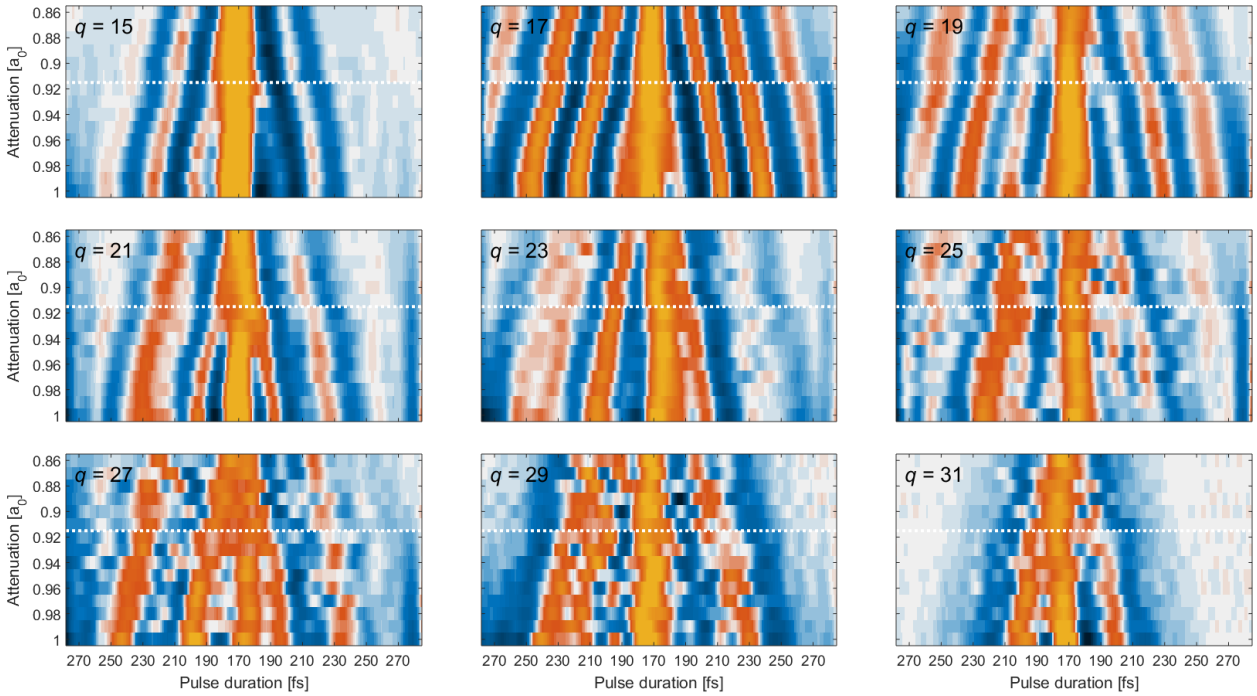

Figure 35: Lineout stacks from the chirp-attenuation scan. The white dotted lines mark the end of the first scan session.

In figure 35 the contrast filtered stacked lineouts of the chirp – attenuation scan are presented. In total 67 fringes, distributed from harmonic 15 to 27, could be traced. The value k, which is the derivative of equation 12 with respect to a, is plotted for each fringe according to harmonic order in figure 36. The average k (just called k from now) is also found in the plot, as the black horizontal line. k will be zero if the following assumptions hold:

1. The IR peak intensity is the only (non-negligible) contributor to the phase difference between long and short trajectory contributions.

2. The compressor position – pulse duration mapping that is used to find the IR pulse duration and IR peak intensity is correct.

Unless some other parameters have contributions to the accumulated phase difference that exactly cancel out with each other or with the effect of an incorrect compressor position – pulse duration mapping, k will be zero only if the assumptions hold. In this case the mapping that was used was obtained from the analysis of an experiment published in [10].

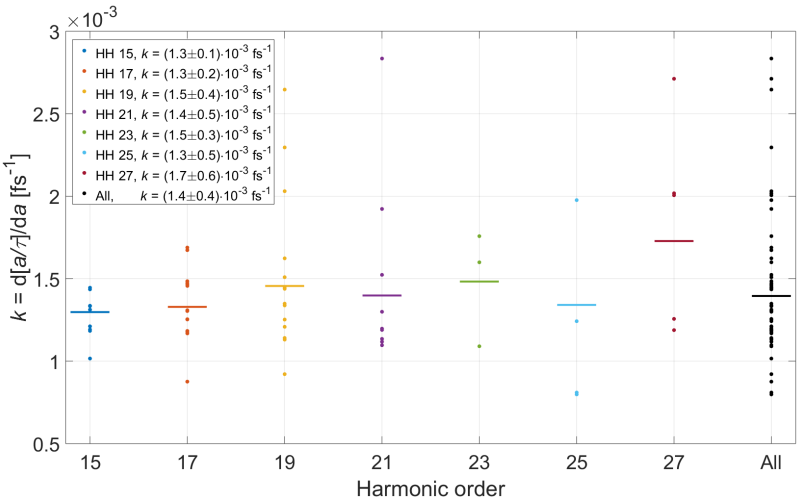

Figure 36: The k values for all traceable fringes in figure 35. The short horizontal lines mark the average k of each harmonic order.

The obtained $k = k_0 \approx (1.4 \pm 0.4) \cdot 10^{-3}\,\mathrm{fs}^{-1}$ is not zero. To check if this could be due to an incorrect compressor position – pulse duration mapping, a fitting parameter p was changed and the process of tracing fringes and finding k was repeated for each new p. p is a parameter that gives the shape of the parabola that maps compressor position to pulse duration. In this scan over p, only fringes seen in harmonic 19 were traced. Harmonic 19 was chosen because it has an average k close to the average of all, k_0, and many traceable fringes. The relation between p and k was found to be approximately linear, and can be seen in figure 37. It turned out that the shape of the parabola had to be tweaked quite a lot to achieve $k = 0$. p had to be decreased so that $p = 0.63p_0$, where p_0 is the initial fitting parameter, to get a vanishing k.

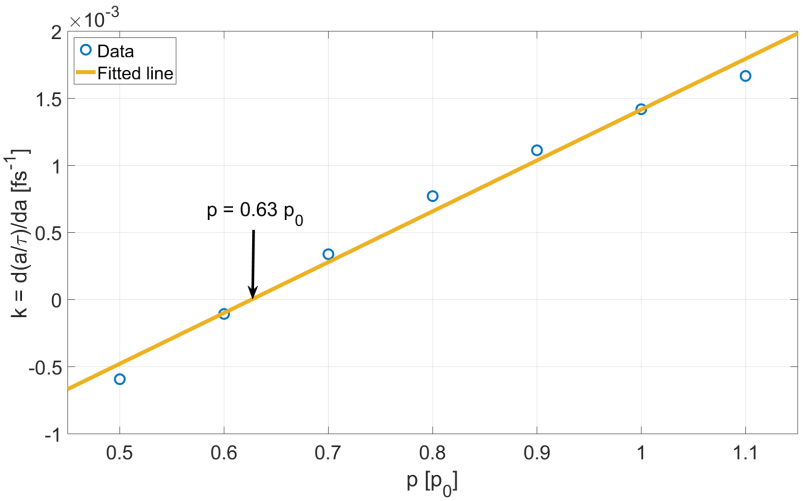

Figure 37: The value k as a function of the fitting parameter p.

In figure 38 the initial parabolic mapping (blue), which was used to obtain figures 35 and 36, can be seen together with the one that is obtained when requiring $k = 0$ (red), i.e., the one with $p = 0.63p_0$. In the figure is also a hyperbola (purple) that has been fitted to data points (yellow) supplied by the laser manufacturer. The reason that a hyperbola has been fitted to these data points is that the relation between pulse duration and compressor position is actually hyperbolic, and not parabolic. The parabolic relation that was used was only ever meant to be an approximation of the hyperbolic relation. Close to minimum pulse duration the approximation should be useful. However, the approximation is not very good in the region of interest; the blue line does not approximate the purple line particularly well. However, the tweaked mapping, which was obtained by fitting the parabolic relation to the data in figure 35, resembles the hyperbola much better. More specifically: in the region were most fringes were traced, i.e., from approximately 200 fs to 300 fs, its slope is very similar to the slope of the hyperbola.

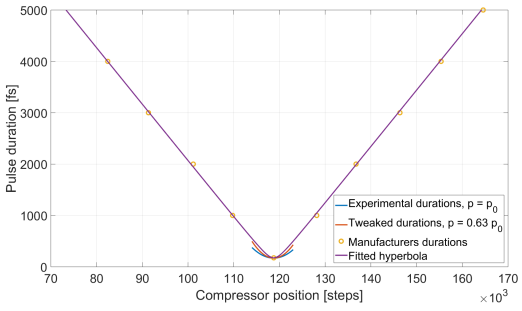

(a) Pulse duration as function of compressor position.

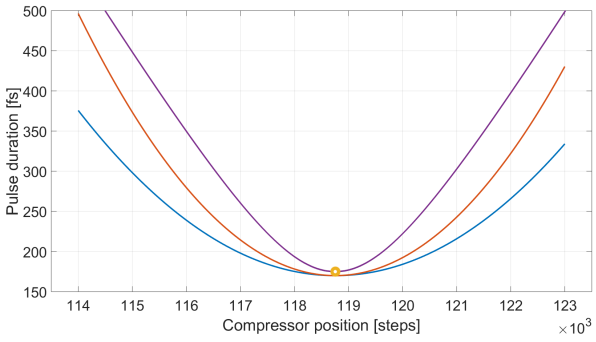

(b) A zoom in of (a).

Figure 38: Different compressor position – pulse duration mappings.

This finding suggests that the original mapping was incorrect and that there are actually better options to use. In other words: it might be that k is non-zero due to assumption (2) above being false, and with

a better compressor position – pulse duration mapping k could be zero and thus assumption (1) proven true. Therefore the process of tracing fringes and finding k was repeated. This time with the manufacturers supplied hyperbolic mapping. With this mapping k was found to be $-0.22 \pm 0.69 \cdot 10^{-3}\,\mathrm{fs}^{-1}$. The interval enclosed by the average value plus-minus its standard deviation contains zero. Therefore assumption (1) has been found to hold, i.e., the intensity of the driving field is the only contributor to the phase difference between long and short trajectory emissions. This is correct conclusion unless some other effects cancel out exactly. In turn this means that a chirp scan is effectively an intensity scan. The k's of all traceable fringes are found in figure 39.

The finding also shows that the compressor position – pulse duration mapping supplied by the manufacturer is correct. Now that it has been shown that the intensity is the only contributor to the phase difference between long and short trajectory emissions, so that k is zero if the mapping is correct, it is possible to go the opposite way; finding the correct mapping by requiring that $k = 0$.

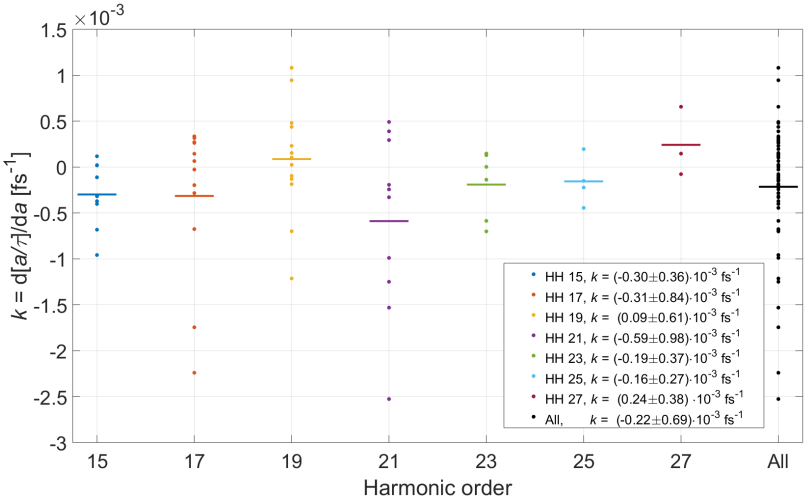

Figure 39: The k values for all traceable fringes in figure 35. The short horizontal lines mark the average k of each harmonic order. Instead of the initial parabolic compressor position – pulse duration mapping the manufacturer's hyperbolic mapping has been used here.

As an extra side note it can be added that the setup shows extraordinary stability. This is manifested in the fact that shutting it down and restarting it 14 hours later only left a small notch in the fringes in figure 35. The break is marked with a white dotted line in the figure. Breaking off a scan into two separate parts is - of course - not a good practice, and should never be encourage, but in this case it at least served to show (off) the stability of the system.

4.4.3 Chirp scan with an MCP filter

The contrast filtered QPI plots in figure 24 look very different depending on whether or not there has been an MCP in the beamline. Those obtained with an MCP has a rapid modulation in the vertical direction, which is absent in the others. Still it is possible to see a resemblance between the two cases, for most harmonic

orders. However, for harmonic 31 the two plots are very different. This has been double-checked and no mistake in the analysis has been discovered. The conclusion of this must be: it is not feasible to put an MCP in the beamline if full QPI plots are needed.

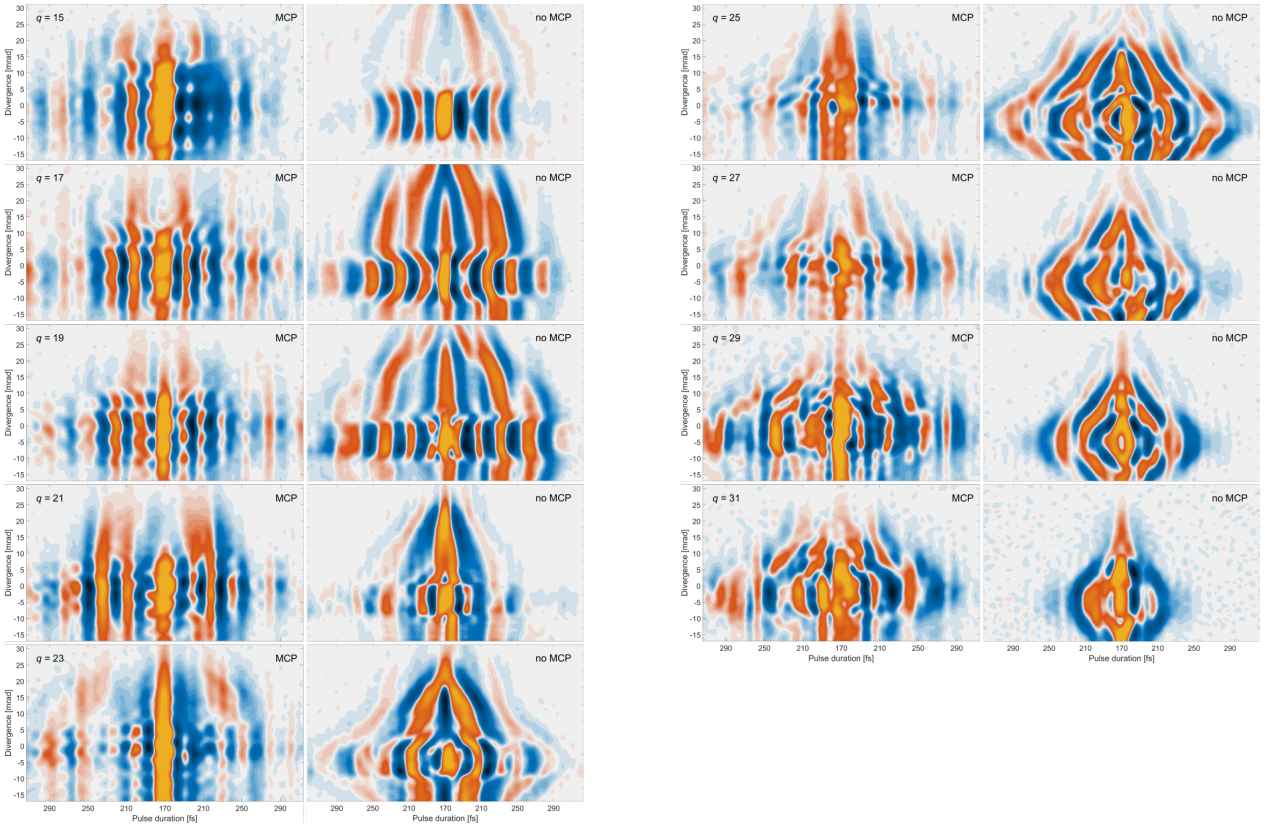

Figure 40: Contrast filtered QPI plots of harmonic 15-31 with and without an MCP filter in the beamline.

If a full QPI plot is not needed, but rather just the central row, then an MCP filter does not have to be a problem. The central row of a MCP filtered QPI plot could still contain the same information as an unfiltered central row. Looking just at the central row is actually the same as tracking the intensity of just one - the central - pixel of a particular harmonic. If it is tracked as two variables is scanned the result is a stacked lineouts plot. That this could be feasible with an MCP in the beamline is indicated by the result in section 4.3, where it is shown that the wavefront of an XUV pulse passing through an MCP is not altered in the central part.

In figure 41 the (vertically) central parts of the contrast filtered QPI plots in figure 24 has been arranged to allow for easy comparison between using and not using an MCP. The similarities are striking, in that most individual fringes in the no MCP plot can be identified, and even found in approximately the same location, in the MCP plots. This means that the phase difference between long and short trajectory contributions has not been altered (much) by passing the MCP. The resemblance is slightly worse in the left halves, which can be due to the laser not being properly warmed up when doing the scan with an MCP. The scans are done from left to right, and therefore if the laser did not reach steady state until approximately half (after ca 20

minutes) the scan was done, this worse resemblance could be the result. The resemblance is also better for the lower order harmonics. For higher order the curvature seen in the fringes obtained without an MCP is absent when using an MCP.

In section 4.3 the wavefront of the central part of the generated XUV pulse, consisting of all harmonics, has been quantified. Here it is also just the central part that is investigated, but for each harmonic separately. Although here the result is not quantified, being just a visual comparison. The reason for this is mainly that the setup was opened and rebuilt between the scans being compared. That action introduced an error of unknown quantity, making a quantitative comparison hard to evaluate. That being said, the conclusion is: for, at least, the lower order harmonics, inserting an MCP in the beam line introduces a change in phase difference between long and short trajectory contributions, in the zeroth order diffraction spot, that is so small that it cannot be easily detected by comparing QPI plots.

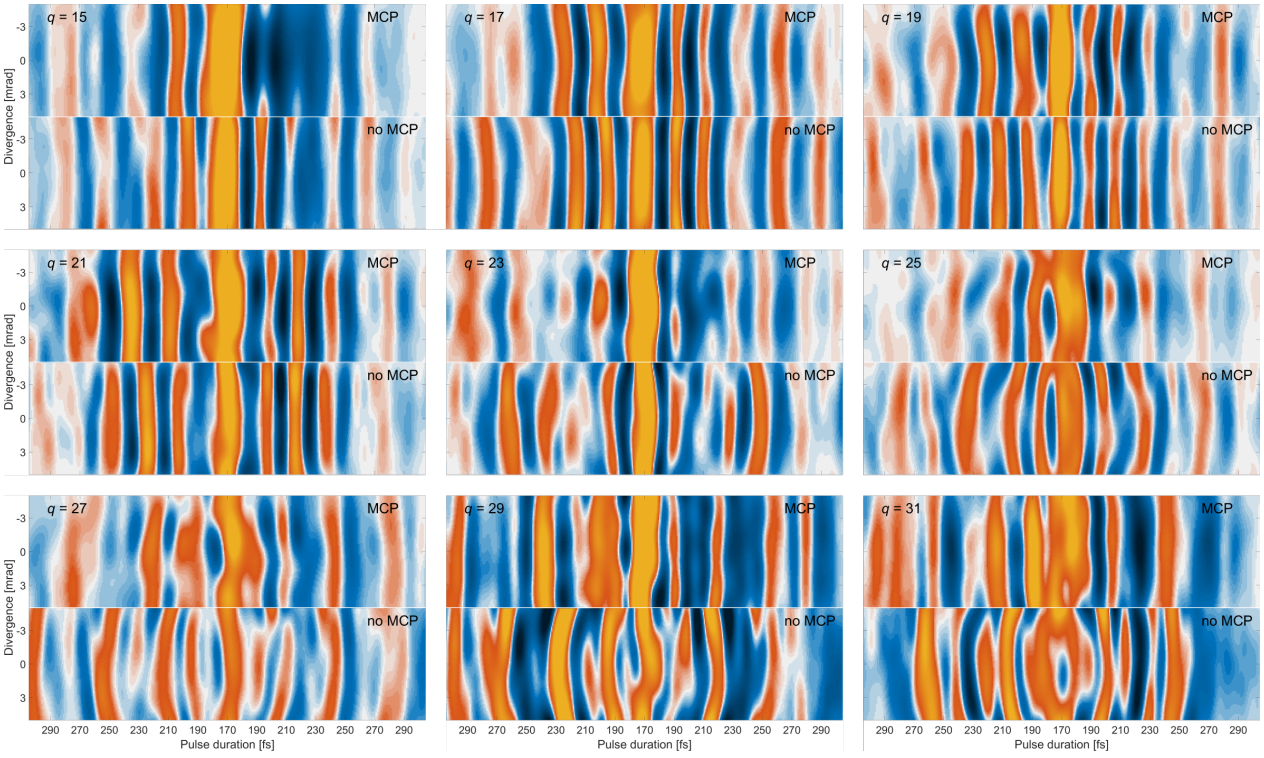

Figure 41: An on axis comparison of the QPI plots in figure 24. Each image shows the central row ± 5 mrad.

When using an MCP filter, the pattern seen on the screen is definitely an interference pattern, and not just a projection of the MCP itself. This being the case is obvious from figure 42, where the detection angle (divergence) of the first order spots is seen to decrease with increasing harmonic order (decreasing wavelength). This is what is expected of an interference pattern, but not by a projection.

All diffraction spots, of a particular harmonic and order, not being equally divergent is due to the horizontal (in x) focusing of the grating. This leads to spots having more of their divergence in the horizontal

plane being detected at a smaller angle than spots having more of their divergence in the vertical plane.

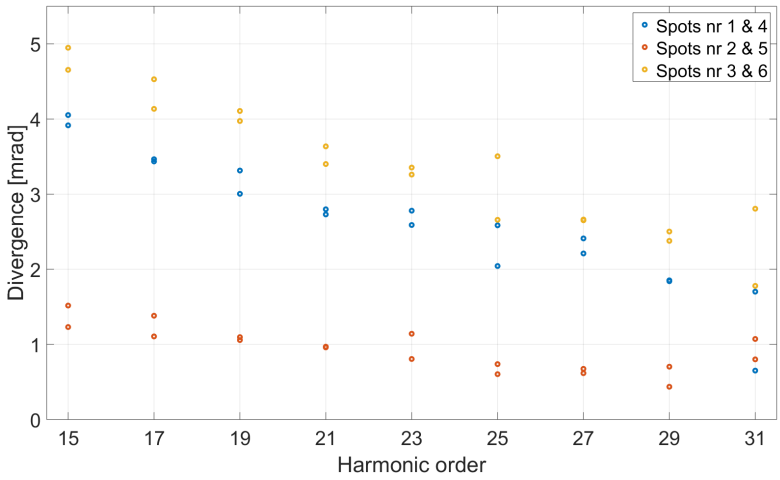

Figure 42: The divergence of the first order diffraction spots as function of harmonic order. The spots are separated into three groups according to their position around the zeroth order spot. How the spots are named can be found in figure 23.

As a final note, inserting an MCP filter in the beamline made the pressure in the detection chamber go down from ca $2.5{\cdot}10^{-5}$ mbar to ca $1.5 \cdot 10^{-6}$ mbar, during experiments. The decrease in pressure was, hence, greater than one order of magnitude and should lead to a longer lifetime for the MCP detector.

4.5 A third source

Trying to simulate the phenomenon of modulated rings, seen in QPI plots, resulted in the lower images in figure 43. In the left image only two wavefronts has been used, while three were used in the one to the right. To just see rings, two interfering wavefronts are sufficient, but to see modulation of them (other than a general decrease in intensity when moving away from the center) it turned out that three sources, i.e., wavefronts, were needed. The letters in the figure indicate particular structures in the data that could be much better replicated when using three sources of interference, instead of just two. Even using three sources the resemblance between simulation and experiment is nowhere near perfect. However, simulation with three interfering wavefronts definitely add the off-axis modulation of the rings that is seen in experiment.

The axes of the experimental and simulated QPI plots are not exactly equal, but that is not necessary if one just wants to show that three sources are needed to obtain the same qualitative appearance in simulations as in experiment. If a quantitative comparison was to be made the axes would, of course, have to be identical.

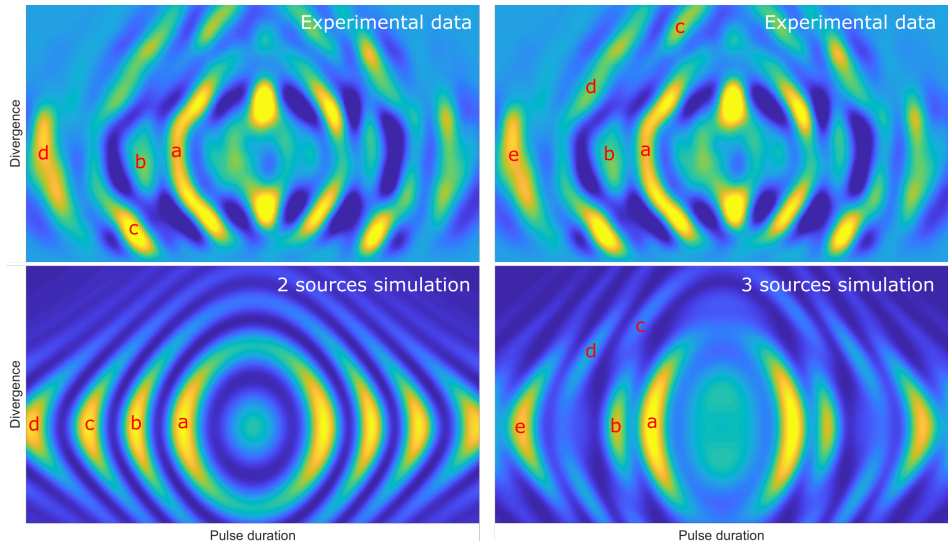

Figure 43: Experimental data and simulations of QPI plots. The upper images are identical and contain actual experimental data, while the lower images are simulations with two and three wavefronts, respectively. The letters indicate structures in the simulations and what they correspond to in the data. The axes for experiment and simulation are not identical.

Whether or not this means that the modulation seen in experiment is actually due to a third trajectory contribution interfering with the short and long trajectory contributions, making this an observation of an HHG trajectory longer than long, remains an open question. The model that is used for the simulation does not manage to replicate long-long interference, probably due to a too simple relation between driving laser intensity and phase of the generated light (see equation 7). Therefore the observed modulation of the rings could also be due to interference within the long trajectory contributions, and not due to a third trajectory. The long trajectory contribution interfering with itself means, in effect, that there are two contributions from long trajectory at each detector position. Adding the short trajectory contribution to that makes three sources of interference. Therefore it can only be stated with confidence that three sources of interference are needed to qualitatively replicate the behavior seen in data, and the model previously used in simulations is, hence, not sufficient. Most likely it has to be upgraded, by adding an other source or/and by adding a more realistic relation between IR intensity and XUV phase.

5 Conclusion

This project has been focused on using an MCP as a filter, and more specifically on whether or not an MCP can be put in the beamline of a setup used for phase sensitive far field experiments. It has also covered a few QPI experiments, which is an example of a phase sensitive far field experiment. This section will go through what has been done, summing it up and repeating the most important conclusions that can be drawn from these experiments.

In the first part shining light through an MCP was simulated using the ray tracing program FRED. The

resulting intensity distributions showed the expected hexagonal interference pattern, associated with MCP's, in the far field. The spots in the pattern were, however, closer to each other than what has been observed in experiments. When focusing the MCP filtered beam, the resulting near field spot looked very similar to that of an unfiltered beam. The filtered beam being well behaved is in agreement with the results presented in [7].

Using a simple setup the divergence and transmittance of visible laser light passing through an MCP were measured. It was found that the divergence of the first order diffraction spots increases linearly with respect to the wavelength, and that the transmission decreases with wavelength. The decrease appears to be exponential, but too few data points were sampled to say anything conclusive about that.

Using a Hartmann sensor the wavefront of the zeroth order diffraction spots of MCP filtered and unfiltered XUV light were characterized. No significant difference between the two cases could be found, using this method. The obtained Zernike coefficients, which characterize the wavefronts, were found to be almost identical. It can therefore be concluded that filtering XUV light with an MCP does not noticeably alter the wavefront of the zeroth order diffraction spot.

When doing the chirp – focal position scan it was found that good QPI contrast was obtained as long as the driving laser was focused after the center of the gas jet. The fringe movement could be approximated by parabolas, which is reasonable, considering the geometry of Gaussian beams. The extreme points of these parabolas must arguably coincide with the laser being focused on the center of the gas jet, and hence the relative position of gas jet and laser focus was found using this method.

To test whether or not chirp scans are effectively attenuation (intensity) scans a chirp – attenuation scan was done. Looking at the QPI plot the fringes moved linearly with the attenuation. This was qualitatively the expected behavior, which would confirm that chirp scans are really extended range intensity scans. However, quantitatively the movement of the fringes was not quite right. When testing if this could be corrected for by a minor adjustment of the parabolic compressor position – pulse duration mapping, it was found that for the relevant pulse duration the adjusted parabolic mapping had a slope very similar to the hyperbolic mapping supplied by the manufacturer of the laser. The analysis of the data was therefore redone, this time using the manufacturers mapping. The resulting fringe movement turned out to be exactly right in this case, and therefore it can be concluded that chirp scans can be used as attenuation (intensity) scans. However, it is important to use the right compressor position – pulse duration mapping to obtain trustworthy results.

An MCP was inserted in the beamline and a chirp scan was done. The resulting spectrum and QPI plot obviously had artifacts, introduced by the MCP. The artifacts could conclusively be said to be a diffraction pattern, and not a mere projection of the MCP, since the divergence of the observed spots increased with wavelength. When looking just at the central parts of QPI plots there was generally a good, although not perfect, resemblance with what is seen when not using an MCP filter. The resemblance turned out to be better for the lower order harmonics. These central parts only consist of the zeroth order diffraction spot. Therefore it was concluded that for the lower order harmonics an MCP filter does not introduce any phase

difference between long and short trajectory contributions in the zeroth order diffraction spot that can be easily detected in a QPI plot.

Finally, off-axis modulation of rings seen in QPI plots of the higher order harmonics called for extra investigation. Trying to simulate the kind of structures that were seen, using only two wavefronts, resulted in a poor resemblance between experiment and simulation. When a third contribution was added to the simulation the resemblance became much better. Specifically the observed behavior of rings being faintest on-axis could be replicated with three contributions, but not at all with just two. Therefore it is suggested that this might possibly be the first ever observation of emission from an HHG electron trajectory longer than long.

6 Outlook

To actually find out if it is feasible to use MCP's as the only mean of removing the driving IR laser, more measurements on the MCP transmittance have to be made. With the MCP's available today the XUV can have a transmittance of up to 60%, while the IR transmittance is roughly 1%. That is far from sufficient to make the initially 100.000 times more intense IR insignificant after filtration. In [7] it is suggested that this should be solved with a smaller MCP hole size. Whether or not this is a viable solution can be investigated by measuring how the XUV and IR transmittance depend on the hole size. It might well be that there is no hole size that both give a low IR to XUV transmittance ratio *and* a high enough XUV transmittance.

The wavefront characterization in this project turned out very conclusive, but to once and for all be able to state that the conclusion regarding this part of the project holds, the result has to replicated and, hence, confirmed.

It was found that chirp scans are really intensity scans, and thus can be used to find the relation between intensity and acquired phase in HHG. This conclusion also has to be confirmed by others. If, however, the conclusion turns out to hold, then chirp scans could be used to gain greater insight in how the intensity of the driving laser affects the phase of the generated XUV light. The experiment and analysis in [10] should basically be redone, but with an improved mapping from laser compressor position to pulse duration. The updated mapping is important, since here it was found that the chirp scan is in effect an intensity scan if the mapping is correct. In close relation to this, the model that is used to fit simulations to acquired data should be updated. It might be that another wavefront must be added for accurate simulations, as indicated in this project. It might also be that the model of the relation between IR intensity and XUV phase has to be made more realistic than, as previously, linear. If it turns out that a more realistic intensity – phase relation is insufficient to replicate the modulation of interference rings in QPI plots, then a big step will have been taken towards confirming the existence and indirect observation of a HHG electron trajectory longer than long.

Acknowledgements

First and foremost I want to acknowledge my supervisors, Prof Johan Mauritsson and Neven Ibrakovic for their support and guidance. Johan, thanks for taking me into your group and for supplying me with a meaningful task and expensive equipment. You've been truly encouraging and enthusiastic throughput the project. It meant a lot to me to be included in social events, even when not formally being part of the group. Neven, it has been a joy to get to know you and to share office with you. Your input has improved the quality of this work quite significantly. All mistakes and errors that remain are solely my own responsibility.

Further, I want to thank Dr Samuel Bengtsson for his absolutely crucial help with the LabVIEW coding, for bringing me to prayer meetings, and for being a great friend in both good and bad (there was one) days. Emma, thanks for helping me out in the lab and for occasionally reminding me about the safety regulations.

I'd also like to thank my family. Hanna, thank you for always standing by my side, for paying the bills, and for showing a reasonable interest in what I do. Ebbe, Elsa, you are amazing. You bring out the best, as well as the worst, in me. Thank you for almost never being sick during the time of this project and for sleeping several times each night. My family, I love you more than I usually show.

Finally, I thank the Creator for making the world so beautiful and intriguing, and for making us able to grasp some of it.

References

[1] M Ferray, Anne L'Huillier, XF Li, LA Lompre, G Mainfray, and C Manus. Multiple-harmonic conversion of 1064 nm radiation in rare gases. *Journal of Physics B: Atomic, Molecular and Optical Physics*, 21(3):L31, 1988.

[2] P ˍ M Paul, ES Toma, P Breger, Genevive Mullot, F Augé, Ph Balcou, HG Muller, and P Agostini. Observation of a train of attosecond pulses from high harmonic generation. *Science*, 292(5522):1689–1692, 2001.

[3] Martin Schultze, Markus Fieß, Nicholas Karpowicz, Justin Gagnon, Michael Korbman, Michael Hofstetter, S Neppl, Adrian L Cavalieri, Yannis Komninos, Th Mercouris, et al. Delay in photoemission. *science*, 328(5986):1658–1662, 2010.

[4] Eiji J Takahashi, Yasuo Nabekawa, Hiroki Mashiko, Hirokazu Hasegawa, Akira Suda, and Katsumi Midorikawa. Generation of strong optical field in soft x-ray region by using high-order harmonics. *IEEE Journal of Selected Topics in Quantum Electronics*, 10(6):1315–1328, 2004.

[5] Edilson L Falcão-Filho, Vasileios M Gkortsas, Ariel Gordon, and Franz X Kartner. Conversion efficiency, scaling and global optimization of high harmonic generation. In *Lasers and Electro-Optics, 2009 and*

2009 Conference on Quantum electronics and Laser Science Conference. CLEO/QELS 2009. Conference on, pages 1–2. IEEE, 2009.

[6] CM Heyl, CL Arnold, A Couairon, and A L'Huillier. Introduction to macroscopic power scaling principles for high-order harmonic generation. *Journal of Physics B: Atomic, Molecular and Optical Physics*, 50(1):013001, 2016.

[7] Qi Zhang, Kun Zhao, Jie Li, Michael Chini, Yan Cheng, Yi Wu, Eric Cunningham, and Zenghu Chang. Suppression of driving laser in high harmonic generation with a microchannel plate. *Optics letters*, 39(12):3670–3673, 2014.

[8] NH Burnett, HA Baldis, MC Richardson, and GD Enright. Harmonic generation in co2 laser target interaction. *Applied Physics Letters*, 31(3):172–174, 1977.

[9] A McPherson, G Gibson, H Jara, U Johann, Ting S Luk, IA McIntyre, Keith Boyer, and Charles K Rhodes. Studies of multiphoton production of vacuum-ultraviolet radiation in the rare gases. *JOSA B*, 4(4):595–601, 1987.

[10] Stefanos Carlström, Jana Preclíková, Eleonora Lorek, Esben Witting Larsen, Christoph M Heyl, David Paleček, Donatas Zigmantas, Kenneth J Schafer, Mette B Gaarde, and Johan Mauritsson. Spatially and spectrally resolved quantum path interference with chirped driving pulses. *New Journal of Physics*, 18(12):123032, 2016.

[11] KJ Schafer, Baorui Yang, LF DiMauro, and KC Kulander. Above threshold ionization beyond the high harmonic cutoff. *Physical review letters*, 70(11):1599, 1993.

[12] Paul B Corkum. Plasma perspective on strong field multiphoton ionization. *Physical Review Letters*, 71(13):1994, 1993.

[13] Maciej Lewenstein, Ph Balcou, M Yu Ivanov, Anne L'huillier, and Paul B Corkum. Theory of high-harmonic generation by low-frequency laser fields. *Physical Review A*, 49(3):2117, 1994.

[14] Chen Guo. *A High Repetition Rate Attosecond Light Source Based on Optical Parametric Amplification*. PhD thesis, Department of Physics, Lund University, 2018.

[15] Maité Louisy, CL Arnold, Miguel Miranda, EW Larsen, Samuel N Bengtsson, David Kroon, Marija Kotur, Diego Guénot, Linnea Rading, Piotr Rudawski, et al. Gating attosecond pulses in a noncollinear geometry. *Optica*, 2(6):563–566, 2015.

[16] Pascal Salieres, Anne L'Huillier, and Maciej Lewenstein. Coherence control of high-order harmonics. *Physical Review Letters*, 74(19):3776, 1995.

[17] B. E. A. Saleh M. C. Teich. *Fundamentals of Photonics*. Wiley, 2 edition, 2007.

[18] Stefanos Carlström. *Sub-Cycle Control of Strong-Field Processes on the Attosecond Timescale*. PhD thesis, Department of Physics, Lund University, 2017.

[19] Maïté Louisy. *Generation of Ultrashort Light Pulses - From Femtosecond to Attosecond*. PhD thesis, Department of Physics, Lund University, 2017.

[20] Esben Witting Larsen, Stefanos Carlström, Eleonora Lorek, Christoph Michael Heyl, D Paleček, Kenneth Joseph Schafer, Anne L'Huillier, Donatas Zigmantas, and Johan Mauritsson. Sub-cycle ionization dynamics revealed by trajectory resolved, elliptically-driven high-order harmonic generation. *Scientific reports*, 6:39006, 2016.

[21] Fabian Brunner. Focus optimization of intense attosecond xuv pulses. Master thesis, Lund University.

[22] RP Photonics Encyclopedia. Chirp. https://www.rp-photonics.com/chirp.html, accessed 2018-11-09.

Appendix

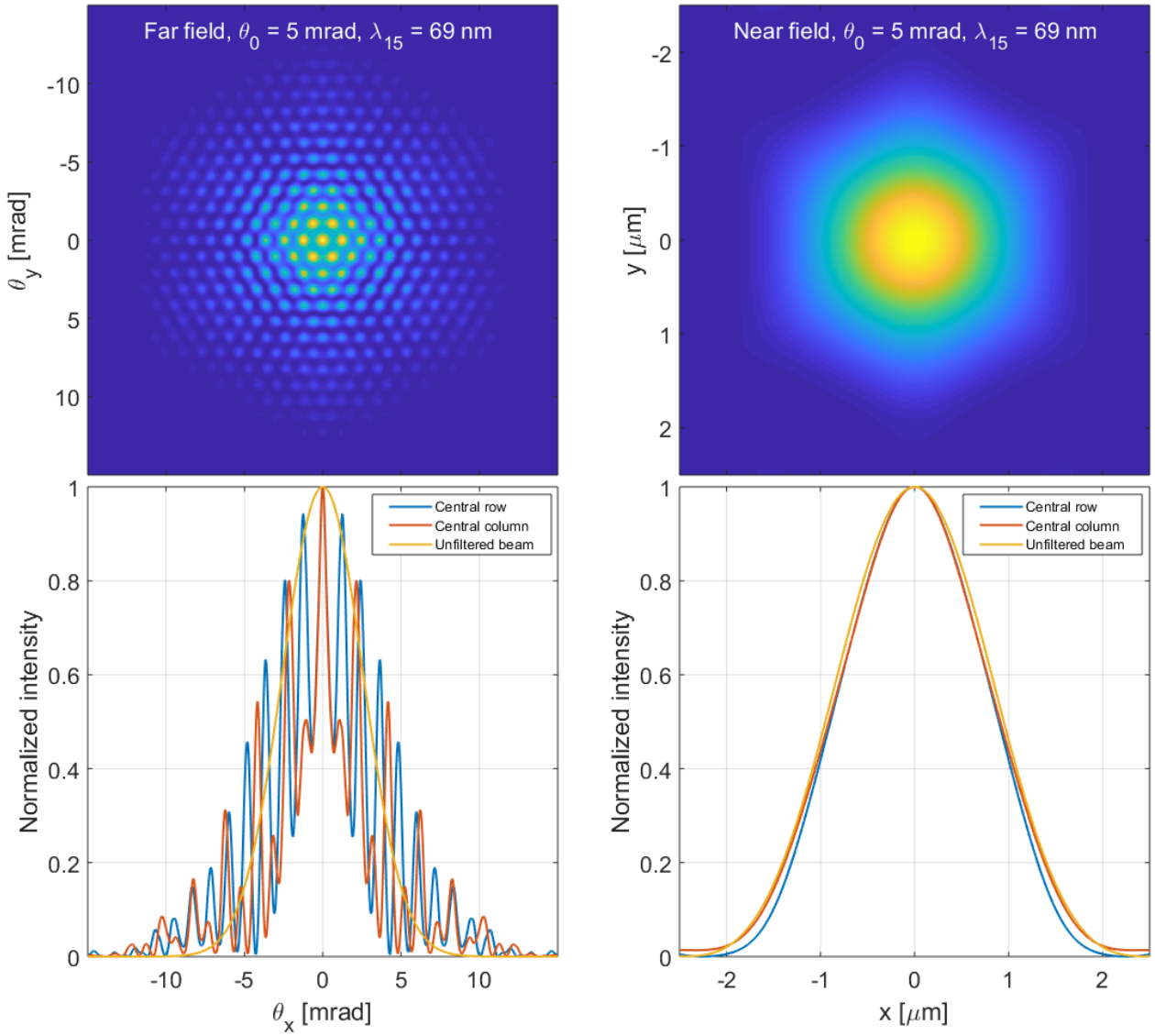

Figure 44: Simulated MCP diffraction patterns, resulting from a Gaussian laser beam with **5 mrad half width divergence** and 69 nm wavelength. Left: The pattern seen in the far field with the central row and column plotted below. Right: The pattern seen in the near field with the central row and column plotted below. In the bottom plots the unfiltered Gaussian beam is added for reference.

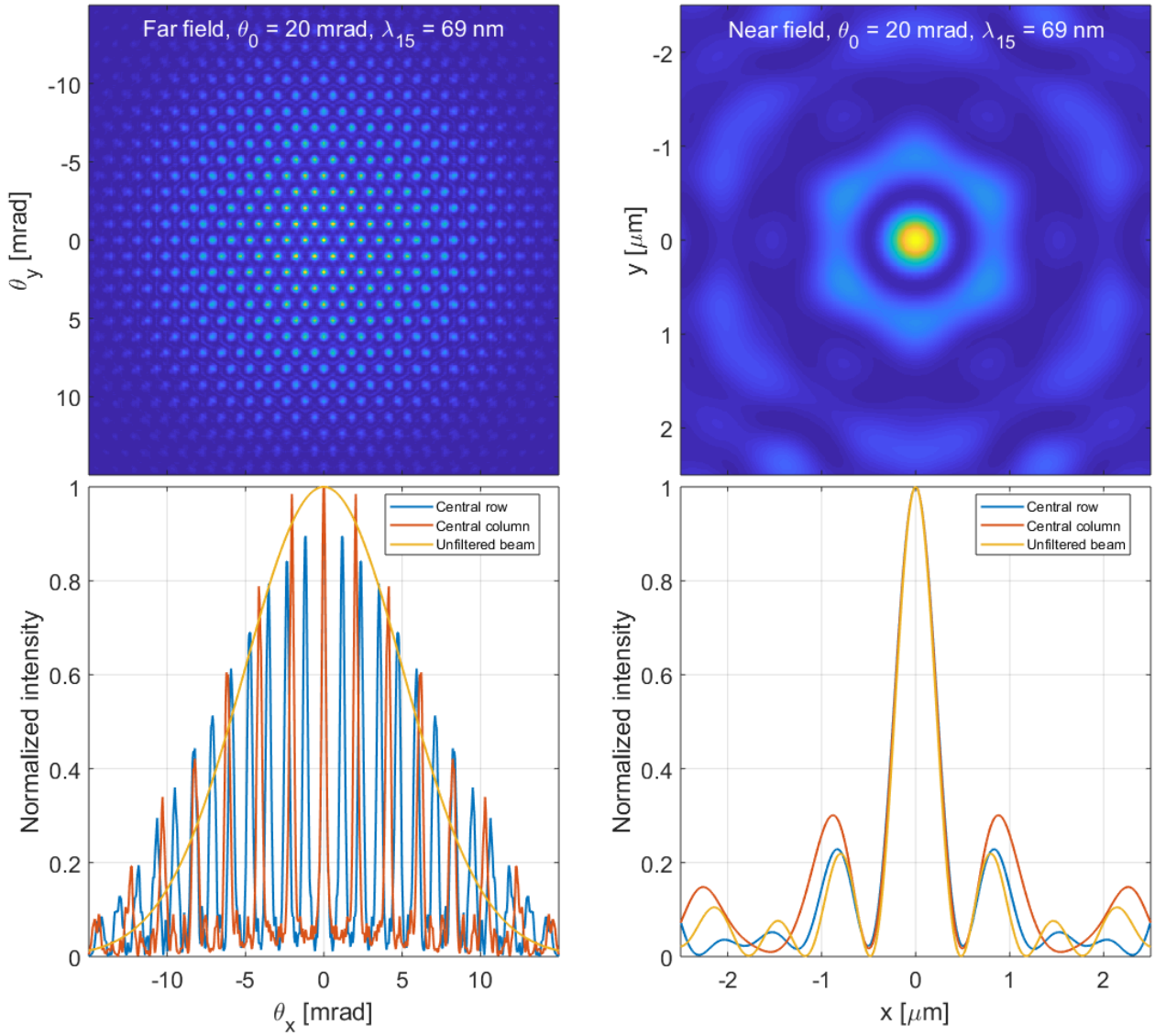

Figure 45: Simulated MCP diffraction patterns, resulting from a Gaussian laser beam with **20 mrad half width divergence** and 69 nm wavelength. Left: The pattern seen in the far field with the central row and column plotted below. Right: The pattern seen in the near field with the central row and column plotted below. In the bottom plots the unfiltered Gaussian beam is added for reference.

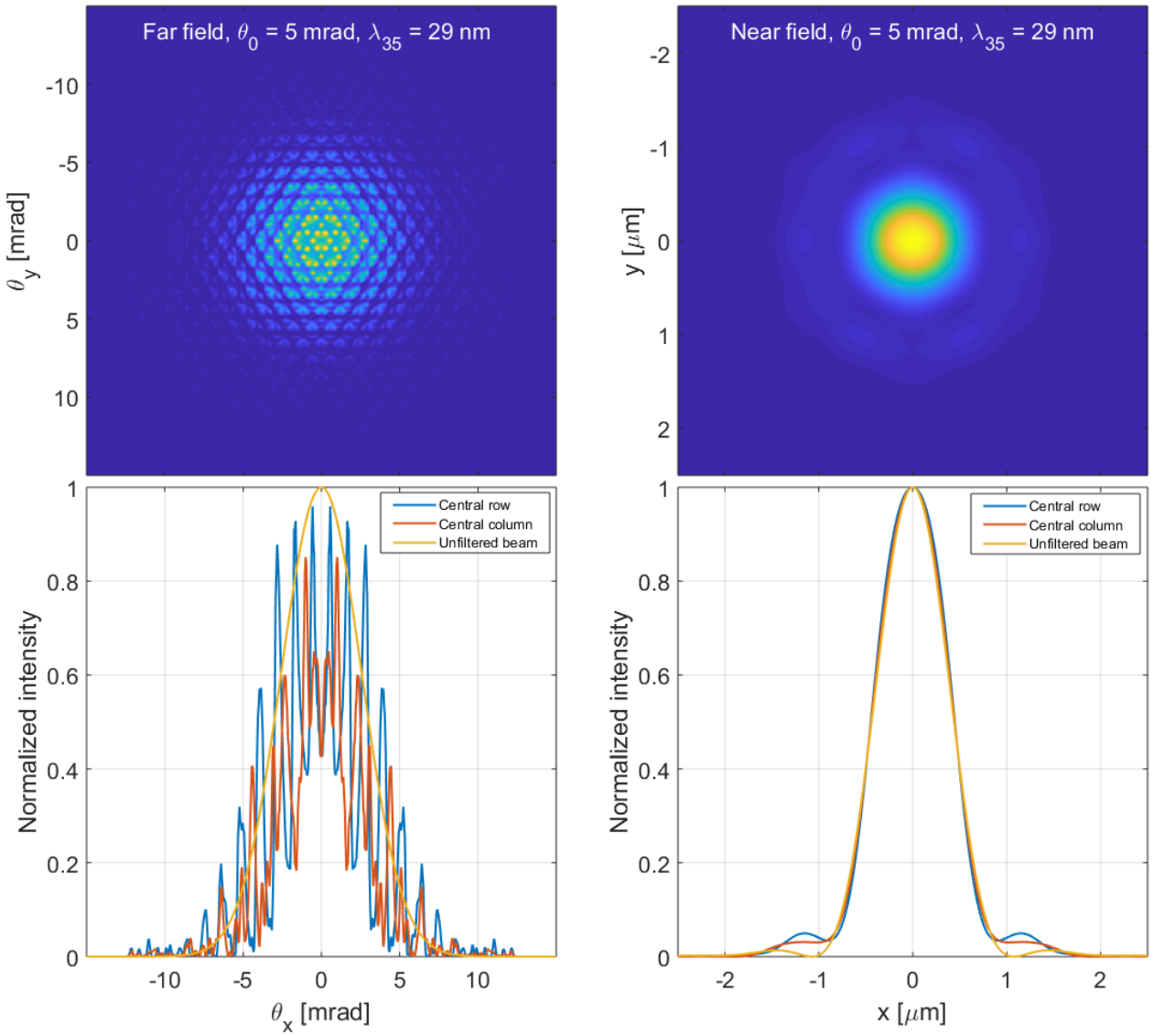

Figure 46: Simulated MCP diffraction patterns, resulting from a Gaussian laser beam with **5 mrad half width divergence** and 29 nm wavelength. Left: The pattern seen in the far field with the central row and column plotted below. Right: The pattern seen in the near field with the central row and column plotted below. In the bottom plots the unfiltered Gaussian beam is added for reference.

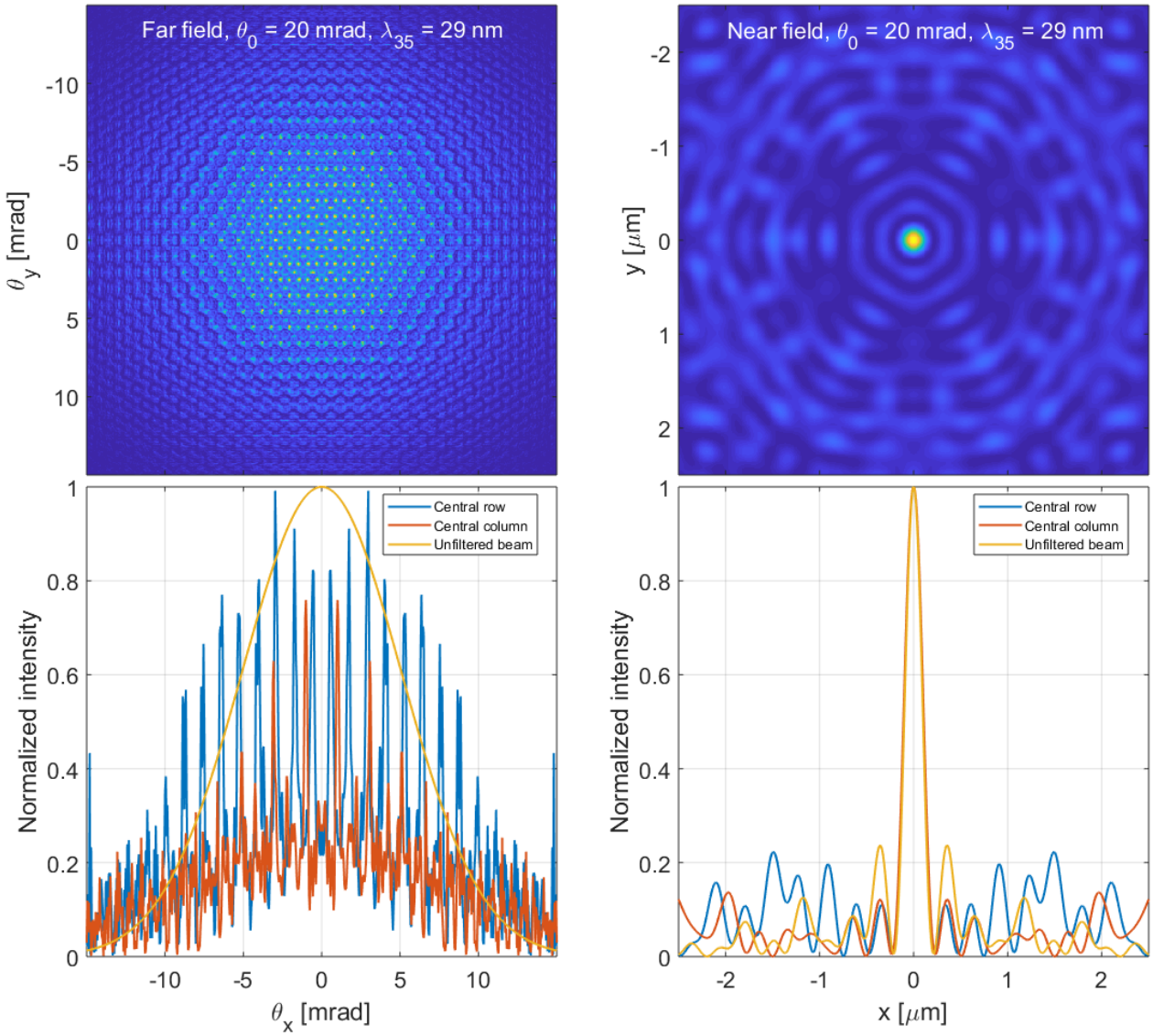

Figure 47: Simulated MCP diffraction patterns, resulting from a Gaussian laser beam with **20 mrad half width divergence** and 29 nm wavelength. Left: The pattern seen in the far field with the central row and column plotted below. Right: The pattern seen in the near field with the central row and column plotted below. In the bottom plots the unfiltered Gaussian beam is added for reference.